A&A, 691, A235 (2024)
https://doi.org/10.1051/0004-6361/202449662

Astronomy & Astrophysics

HYPERION. Shedding light on the first luminous quasars: A correlation between UV disc winds and X-ray continuum

A. Tortosa[1,⋆], L. Zappacosta[1], E. Piconcelli[1], M. Bischetti[2,3], C. Done[4], G. Miniutti[5], I. Saccheo[6,1], G. Vietri[7], A. Bongiorno[1], M. Brusa[8,9], S. Carniani[10], I. V. Chilingarian[14], F. Civano[11], S. Cristiani[2,12,13], V. D'Odorico[2,10,12], M. Elvis[14], X. Fan[15], C. Feruglio[2,12], F. Fiore[2,12], S. Gallerani[10], E. Giallongo[1], R. Gilli[9], A. Grazian[16], M. Guainazzi[17], F. Haardt[18,19,20], A. Luminari[21,1], R. Maiolino[22,23,24], N. Menci[1], F. Nicastro[1], P. O. Petrucci[25], S. Puccetti[26], F. Salvestrini[2], R. Schneider[1,27,28,29], V. Testa[1], F. Tombesi[30,31,1,32,11], R. Tripodi[33,2,3,12], R. Valiante[1,28], L. Vallini[9], E. Vanzella[9], A. Vasylenko[34], C. Vignali[8,9], F. Vito[9], M. Volonteri[35], and F. La Franca[6,1]

(Affiliations can be found after the references)

Received 19 February 2024 / Accepted 16 September 2024

ABSTRACT

One of the main open questions in the field of luminous ($L_{\rm bol}$>10^{47} erg s^{-1}) quasars (QSOs) at $z \gtrsim 6$ is the rapid formation (<1 Gyr) of their supermassive black holes (SMBHs). For this work we analysed the relation between the X-ray properties and other properties describing the physics and growth of both the accretion disc and the SMBH in QSOs at the Epoch of Reionization (EoR). The sample consists of 21 $z > 6$ QSOs, which includes 16 sources from the rapidly grown QSOs from the HYPERION sample and five other luminous QSOs with available high-quality archival X-ray data. We discovered a strong and statistically significant (>3σ) relation between the X-ray continuum photon index (Γ) and the C IV disc wind velocity ($v_{\rm C\,IV}$) in $z > 6$ luminous QSOs, whereby the higher the $v_{\rm C\,IV}$, the steeper the Γ. This relation suggests a link between the disc–corona configuration and the kinematics of disc winds. Furthermore, we find evidence at $>2-3\sigma$ level that Γ and $v_{\rm C\,IV}$ are correlated to the growth rate history of the SMBH. Although additional data are needed to confirm it, this result may suggest that, in luminous $z > 6$ QSOs, the SMBH predominantly grows via fast accretion rather than via initial high seed BH mass.

Key words. galaxies: active – galaxies: high-redshift – galaxies: nuclei – quasars: general – quasars: supermassive black holes – X-rays: galaxies

1. Introduction

The study of luminous ($L_{\rm bol} \gtrsim 10^{47}$ erg s^{-1}) quasars (QSOs) at $z > 6$, hosting supermassive black holes (SMBHs) with black hole masses $M_{\rm BH} > 10^8\,M_\odot$ up to $10^{10}\,M_\odot$ (Volonteri 2010; Wu et al. 2011, 2015; Johnson & Haardt 2016; Valiante et al. 2017; Bañados et al. 2018; Yang et al. 2020; Wang et al. 2021b; Eilers et al. 2023; Fan et al. 2023; Zappacosta et al. 2023; D'Odorico et al. 2023, and references therein), offers a unique window to investigate their formation and rapid growth in the short time interval available (<1 Gyr). The formation of SMBH on a relatively short timescale is still an open question and, assuming the formation of high-z SMBH progenitors at $z \approx 20-30$ (Johnson & Haardt 2016), different scenarios have been presented to explain the presence of a $10^9\,M_\odot$ SMBH at $z > 6$. They either involve the presence of a massive BH seed ($M_{\rm BH}^{\rm seed} > 10^{3-4}\,M_\odot$) regardless of the subsequent accretion rate and/or a series of short and intermittent super-Eddington accretion phases allowing the growth from lower BH mass seeds ($M_{\rm BH}^{\rm seed} \sim 100\,M_\odot$) (Lupi et al. 2016; Inayoshi et al. 2020). Currently there are no conclusive indications towards one scenario or the other. If, on the one hand, the existence of a local population of active intermediate-mass BH ($10^{4.5-5.2}\,M_\odot$) in the local Universe (Reines et al. 2013; Chilingarian et al. 2018; Greene et al. 2020) may support stellar mass BH seeds for their origin (Mezcua 2017), on the other hand, the observation at $z \gtrsim 10$ of BHs with $M_{\rm BH} \gtrsim 10^6\,M_\odot$, direct progenitors of the first ($z > 6$) luminous QSOs, still cannot provide conclusive evidence for their origin (Maiolino et al. 2024; Bogdán et al. 2024).

Information about the accretion process of SMBHs can be obtained by exploring the innermost regions of luminous QSOs, for example through X-ray spectroscopy. X-ray emission arising from SMBHs, powering active galactic nuclei (AGN) and luminous QSOs, in particular, is believed to be produced by the interplay between the accretion disc (AD) and the corona, called the 'two-phase model' (Haardt & Maraschi 1991). Thermal UV/optical photons emitted from the AD are inverse-Compton scattered by the coronal hot relativistic electrons into the X-rays, creating a primary X-ray continuum (e.g. Sunyaev & Titarchuk 1980; Haardt & Maraschi 1993) with the spectral shape of a power law characterized by a photon index, Γ, and a cut-off at high energy, $E_{\rm cut}$, both related to the physical characteristics of the corona (i.e. coronal temperature, $kT_{\rm e}$, and optical depth, τ). This high-energy radiation is a direct manifestation of the extreme conditions near the central SMBH, and it carries essential information about the innermost regions of the AGN, the mechanisms governing their accretion process and ultimately the SMBH growth. The photon index of the primary power law is a possible proxy of the AGN accretion rate, parametrized by the Eddington ratio: the ratio of the bolometric luminosity to the Eddington luminosity, $\lambda_{\rm Edd} = \frac{L_{\rm bol}}{L_{\rm Edd}}$. However, the presence of a $\Gamma-\lambda_{\rm Edd}$ relation, according to which very steep Γ are commonly detected in highly accreting AGN, has been largely debated (Trakhtenbrot et al. 2017; Liu et al. 2021;

⋆ Corresponding author; alessia.tortosa@inaf.it

Laurenti et al. 2022; Kamraj et al. 2022; Trefoloni et al. 2023; Tortosa et al. 2023).

There are many observational works dedicated to the X-ray spectroscopy of $z > 6$ QSOs so far (e.g. Gallerani et al. 2017; Bañados et al. 2018; Salvestrini et al. 2019; Pons et al. 2019; Vito et al. 2019, 2021; Connor et al. 2019, 2020; Wang et al. 2021a; Yang et al. 2022; Zappacosta et al. 2023, and references therein). In particular, Zappacosta et al. (2023) reports the result of the X-ray analysis of the first year of a *XMM-Newton* Multi–Year Heritage programme dedicated to the HYPerluminous quasars at the Epoch of ReionizatION, (HYPERION) sample, which consists of 18 $z > 6$ luminous ($L_{\rm bol} > 10^{47}\,{\rm erg\,s^{-1}}$) QSOs, known by 2020, and powered by SMBHs that appear to have undergone the fastest SMBH formation compared to other coeval sources. Assuming continuous exponential growth via accretion at $\lambda_{\rm Edd} = 1$, these QSOs require an initial $M_{\rm BH}^{\rm seed} > 1000\,M_{\odot}$, assuming that the formation of their seeds happend at $z = 20$, e.g. Valiante et al. (2016). Zappacosta et al. (2023) found that the X-ray photon index is, on average, significantly steeper than that of $z < 6$ QSOs that are analogues in terms of luminosity and $\lambda_{\rm Edd}$ therefore suggesting a redshift evolution in the nuclear properties of the first QSOs (see also Vito et al. 2019; Wang et al. 2021b).

Luminous QSOs are also expected to show the presence of powerful winds at all scales (e.g. Faucher-Giguère & Quataert 2012; Shen & Ho 2014; Fiore et al. 2017). In particular, AD winds traced by broad C IV emission lines have been discovered with velocities, corresponding to the relative shift between the peak of the C IV and Mg II emission lines, up to $v_{\rm C\,IV} \sim -8000$ km/s (Shen et al. 2016). The $v_{\rm C\,IV}$ parameter is found to correlate with the QSOs accretion rate (Richards et al. 2011; Marziani et al. 2016; Vietri et al. 2018; Rankine et al. 2020; Timlin et al. 2020; Temple et al. 2021). Notably, Zappacosta et al. (2020) reported an anti-correlation between $v_{\rm C\,IV}$ and the intrinsic 2–10 keV luminosity ($L_{\rm X}$) for a sample of luminous ($L_{\rm bol} > 10^{47}\,{\rm erg\,s^{-1}}$) $z = 2 - 4$ QSOs with similar UV luminosity. This suggests a connection between the AD winds and the X-ray emission whereby the stronger winds are hosted in weaker X-ray sources.

For this work we explored for the first time the relations between the X-ray nuclear properties (i.e. Γ and $L_{\rm X}$), the C IV velocity shift, the C IV rest-frame equivalent width (REW$_{\rm C\,IV}$) and properties regarding the physics and growth of the AD and the SMBH, in a sample of luminous QSOs at $z \sim 6$–7.5. The paper is organized as follows. In Section 2, we present the sample and we describe the data reduction processes. In Section 3 we present the spectral and correlation analysis performed in this work. In Section 4 we describe the results of our analysis, which are discussed in Section 5 and summarized in Section 6.

Standard cosmological parameters ($H = 70\,{\rm km\,s^{-1}\,Mpc^{-1}}$, $\Omega_{\Lambda} = 0.73$ and $\Omega_{\rm m} = 0.27$) are adopted throughout the paper. Errors are reported at the 68% confidence level with upper and/or lower limits quoted at the 90% confidence level.

2. Sample selection and data presentation

2.1. The sample

The sample considered in this work includes all known $z > 6$, $L_{\rm bol} \gtrsim 10^{47}\,{\rm erg\,s^{-1}}$ QSOs detected with >30 total X-ray net counts (0.3–7 keV) and with available measurements of $v_{\rm C\,IV}$ from the literature. It consists of 16 HYPERION QSOs with X-ray data from the *XMM-Newton* Multi–Year Heritage programme obtained by August 2023 and five other QSOs with available archival good–quality X-ray data from Connor et al. (2019),Vito et al. (2019) and Pons et al. (2020). The list of all 21 QSOs and their general properties is reported in Table 1. We included in the analysis the most recent *XMM-Newton* data of the HYPERION source ATLAS J029-36 (OBSID 0930591101 and 0930591201, P.I. Norbert Schartel), which helped us to improve considerably the data quality of the HYPERION dataset.

For our QSO sample we introduced the seed mass parameter assuming accretion at the Eddington limit ($\lambda_{\rm Edd} = 1$), $M_{\rm s,Edd}$, defined using the exponential relation

$$M_{\rm s,Edd} = M_{\rm BH} \times e^{-t/t_s} \quad (1)$$

where t is the elapsed time between the formation redshift of the seed BH and the redshift at which the QSO is observed and t_s is the e-folding time: $t_s = 0.45\eta(1-\eta)^{-1}\lambda_{\rm Edd}^{-1}f_{\rm duty}^{-1}$ [Gyr]. In this calculation we assumed that seed BHs form at $z = 20$ (Valiante et al. 2016) and continuously accrete at the Eddington limit, with radiative efficiency, representing the fraction of accreted mass which is radiated, $\eta = 0.1$, and with duty cycle (i.e. the fraction of the time during which the AGN is active, $f_{\rm duty} = 1$) corresponding to a continuous active phase. This quantity can be considered as a proxy for the SMBH growth rate: the larger $M_{\rm s,Edd}$, the higher the expected growth rate.

We note that the HYPERION QSOs have BH masses computed from single-epoch MgII-based estimation (Vestergaard & Osmer 2009). For some of the HYPERION QSOs (i.e. VHS J0411−0907 and VDES J0020−3653 (Marshall et al. 2023); VDES J0244-5008 and VDES J0224-4711 (Yang et al. 2023); SDSS J0100+2802 (Eilers et al. 2023) Hβ-based BH masses estimates from the *James Webb* Space Telescope (JWST) are now available. However, the Hβ-based BH masses are consistent with MgII-based masses, ensuring statistically the reliability of $M_{\rm s,Edd}$ estimates.

Within the *XMM-Newton* Multi-Year Heritage programme, most of the sources have observations during multiple epochs. We consistently reduced and analysed all the *XMM-Newton* data of the 16 HYPERION QSOs, as well as the available *XMM-Newton* data of PSO J159-02 and SDSS J1030+0524, two of the five additional non-HYPERION sources in our sample. The X-ray data reduction and their spectral analysis are described in Sections 2.2 and 3.1, respectively. For the remaining three QSOs, which only have *Chandra* observations available, we used data from the literature.

Regarding $v_{\rm C\,IV}$ and REW$_{\rm C\,IV}$, there are multiple values in the literature of both parameters, measured with different fitting approaches (see Section 2.3 and Table 3). In this work, we took into account all the available measures in the literature of $v_{\rm C\,IV}$ and/or REW$_{\rm C\,IV}$ (see Section 3.2 for more details).

2.2. X-ray data reduction

We reported the details of the HYPERION observations, both archival and from the *XMM-Newton* Multi-Year Heritage X-ray programme (up to August 2023) in the upper part of Table 2. The available *XMM-Newton* observations of the non-HYPERION QSOs belonging to our sample are reported in the lower part of Table 2.

The data reduction was performed following the same approach as Zappacosta et al. (2023). The event lists of the EPIC-pn (Strüder et al. 2001) and EPIC-MOS (Turner et al. 2001) detectors are extracted with the `epproc` and `emproc` tools of the standard System Analysis Software (`SAS` v.18.0.0; Gabriel et al. 2004). The latest calibration files available by

Table 1. Sample of $z > 6$, luminous QSOs considered in this work, along with their accretion and C IV emission properties.

Target	z [a]	$\log(L_{\rm bol})$ [b] [erg s^{-1}]	$\log(M_{\rm BH})$ [c] [$M_\odot$]	$\lambda_{\rm Edd}$	$\log(M_{\rm s,Edd})$ [c] [$M_\odot$]	$v_{\rm C\,IV}$ [d] [km s^{-1}]	REW$_{\rm C\,IV}$ [d] [Å]	Ref.
HYPERION QSOs: *XMM-Newton* Heritage programme								
ULAS J1342+0928	7.541	47.19 ± 0.01	8.90 ± 0.14	1.58	4.28 ± 0.12	−5633 ± 828	17.04 ± 1.04	1
J1007+2115	7.494	47.30 ± 0.02	9.18 ± 0.05	1.06	4.51 ± 0.05	−3201 ± 918	10.00 ± 1.60	1
ULAS J1120+0641	7.087	47.30 ± 0.21	9.41 ± 0.11	0.61	4.26 ± 0.10	−2276 ± 183	31.05 ± 1.70	1
DES J0252−0503	6.99	47.12 ± 0.04	9.15 ± 0.05	0.74	3.88 ± 0.05	−4354 ± 762	17.30 ± 1.00	1
VDES J0020−3653	6.834	47.16 ± 0.01	9.24 ± 0.08	0.66	3.75 ± 0.09	−1700 ± 100	55.00 ± 1.00	1
VHS J0411−0907	6.824	47.31 ± 0.02	8.80 ± 0.04	2.57	3.30 ± 0.04	−1418 ± 298	43.20 ± 4.80	1
VDES J0244−5008	6.724	47.19 ± 0.01	9.08 ± 0.15	1.02	3.45 ± 0.18	−3200 ± 310	24.00 ± 2.00	1
PSO J231.6−20.8	6.587	47.31 ± 0.01	9.50 ± 0.09	0.51	3.67 ± 0.08	−3829 ± 116	6.66 ± 2.00	1, 5
PSO J036.5+03.0	6.533	47.33 ± 0.05	9.49 ± 0.12	0.55	3.58 ± 0.14	−4477 ± 326	20.78 ± 0.90	1, 5
VDES J0224−4711	6.526	47.53 ± 0.01	9.36 ± 0.08	1.18	3.43 ± 0.09	−1814 ± 258	50.25 ± 2.00	1, 5
PSO J011+09	6.444	47.12 ± 0.01	9.15 ± 0.15	0.74	3.10 ± 0.18	−3356 ± 338	7.38 ± 1.75	1, 6
SDSS J1148+5251	6.422	47.57 ± 0.01	9.74 ± 0.03	0.54	3.66 ± 0.001	−2803 ± 51	44.68 ± 2.46	1, 6
SDSS J0100+2802	6.300	48.24 ± 0.04	10.04 ± 0.27	1.26	3.76 ± 0.04	−2496 ± 316	5.11 ± 0.50	1, 5
ATLAS J025−33	6.294	47.39 [*]	9.43 ± 0.21	0.73	3.14 ± 0.27	−3246 ± 295	18.82 ± 1.50	1, 8
CFHQS J0050+3445	6.246	47.29 ± 0.01	9.68 [*]	0.32	3.31 [*]	864 ± 487	63.68 ± 2.60	1
ATLAS J029−36	6.027	47.39 [*]	9.82 [*]	0.30	3.08 [*]	−2178 ± 267	14.59 ± 1.90	1, 8
Non-HYPERION QSOs								
PSO J159−02	6.38 [†]	47.29 ± 0.01	9.51 ± 0.05	0.30	3.32 ± 0.05	−726 ± 120	54.70 ± 3.82	4, 6, 7
SDSS J1030+0524	6.308	47.14 ± 0.14	9.29 ± 0.10	0.57	3.02 ± 0.11	−876 ± 235	32.77 ± 2.37	2, 5
PSO J308−21	6.24 [†]	47.37 ± 0.01	9.24 ± 0.07	1.40	2.83 ± 0.08	−2003 ± 233	35.15 ± 1.61	3, 6
SDSS J1602+4228	6.09 [⋆]	47.03 [*]	9.37 [*]	0.62	2.57 [*]	−311 ± 479	59.19 ± 3.23	2, 5
SDSSJ1306+0356	6.034 [†]	47.12 ± 0.01	9.31 ± 0.07	0.48	2.59 ± 0.12	−786 ± 111	47.89 ± 1.76	2, 5

Notes. [a]z estimated from the Mg II emission line if not stated otherwise; [b]estimated from luminosity 3000 Å (Richards et al. 2006); [c]for the HYPERION sources we report the values of the $M_{\rm BH}$ and the estimated $M_{\rm s,Edd}$ from Zappacosta et al. (2023), for the Non-HYPERION from Mazzucchelli et al. (2023), Farina et al. (2022) re-scaled using the same cosmological estimators as in Zappacosta et al. (2023), if present; [d]when more than one $v_{\rm C\,IV}$ and REW$_{\rm C\,IV}$ values is present in the literature, for simplicity, we report the mean values derived using all the available values reported in Table 3, the errors are the mean of the errors. We note that the correlation analysis takes into account all the existing values of $v_{\rm C\,IV}$ (see Section 3.2). [†]z estimated from the [C II] emission line. [⋆]z estimated from the Ly α emission line. [*]Error not reported in the literature. (1) Zappacosta et al. (2023); (2) Vito et al. (2019); (3) Connor et al. (2019); (4) Pons et al. (2020); (5) Mazzucchelli et al. (2023); (6) Farina et al. (2022) (7) Schindler et al. (2020); (8) Chehade et al. (2018).

August 2023 were used. The choice of the optimal time cuts for flaring particle background was performed visually inspecting light curves created in the 10–12 keV (EPIC-pn) and >10 keV (EPIC-MOS) energy ranges, with PATTERN=0 (single events). For the choice of the source and background extraction radii, we identified the point-like sources in each target field of view running the meta-task `edetect-chain` on the 0.5−2 keV energy band EPIC images by setting a detection maximum likelihood threshold DETML = 6 (DETML = $-\ln P_{\rm rnd}$ where $P_{\rm rnd}$ is the probability of detection by chance). We selected as source region a circular region with a radius of 20 arcsec (corresponding to ∼80% of the on-axis PSF encircled energy fraction at 1.5 keV), centred on each published optical target position. Since VDES J0244−5008 and VDES J0020−3653 had a nearby source distant 28 arcsec and 17 arcsec, respectively, we adopted a smaller source region of 15 arcsec and 12 arcsec radius (∼65%−70% of the encircled energy fraction), respectively. As background regions, we adopted for the EPIC-pn camera rectangular regions with long and short sides in the range 3.6–3.9 arcmin and 1.9–2.7 arcmin, respectively, located around the source region and rotated with the same position angle of the detector. For the two EPIC-MOS detectors, we adopted as background regions circular regions of radius in the range 2.5–3.4 arcmin centred on the target position. From all the background regions we excluded circular regions with a radius of 40 arcsec centred on the target position and on all the contaminant point sources previously identified. Response matrices and auxiliary response files were generated using the `SAS` tasks `rmfgen` and `arfgen`, respectively. Spectral data were binned using the optimal Kaastra & Bleeker 2016 (hereafter KB) grouping, which provides the optimal binning for data and model accounting for the source spectral shape, the variable spectral resolution and the average photon energy in each bin. The KB grouping is the best scheme to recover unbiased energy independent spectral parameter estimates for low count regime spectra of $z > 6$ sources (see Appendix B in Zappacosta et al. 2023 for further details).

2.3. C IV velocity shift

The shift in the peaks of high-ionization broad emission lines, such as C IV, relative to the source systemic redshift, is usually interpreted as a signature of AD-driven broad-line winds (Elvis 2000; Leighly 2004) at both low redshifts (e.g. Richards et al. 2002) and high redshifts (e.g. De Rosa et al. 2014).

The presence of C IV shifts in luminous QSOs with respect to the systemic redshift determined by lower ionization broad lines (e.g. Mg II) or host narrow lines (e.g. [O III], CO, [C II]) has been widely investigated, and the position of the C IV line has been determined using the line velocity centroid (e.g. Mortlock et al.

Table 2. *XMM-Newton* observations analysed in this work.

OBSID	Target	RA (J2000)	Dec (J2000)	Start date (UTC)	Exp. [ks]	Net exp. PN [ks]	Net exp. MOS1 [ks]	Net exp. MOS2 [ks]
HYPERION QSOs: archival observations								
0790180701	SDSS J0100+2802	01:00:13.02	+28:02:25.8	2016-06-29	65.00	44.85	59.92	56.00
0824400301	VDES J0224−4711	02:24:26.54	−47:11:29.4	2018-05-25	35.00	13.87	27.81	24.73
0930591101	ATLAS J029−36	01:59:57.97	−36:33:56.6	2024-06-10	135.00	61.79	75.03	78.02
0930591201	ATLAS J029−36	01:59:57.97	−36:33:56.6	2024-06-12	135.00	67.98	86.07	91.11
HYPERION QSOs: *XMM-Newton* Heritage programme QSOs								
0884992601	CFHQS J0050+3445	00:50:06.67	+34:45:22.6	2021-06-26	45.00	26.38	37.39	29.66
0884990401	ULAS J1120+0641	11:20:01.48	+06:41:24.3	2021-06-27	73.00	36.08	56.27	55.38
0884990101	ULAS J1342+0928	13:42:08.10	+09:28:38.6	2021-07-05	106.50	60.51	82.48	68.38
0884992101	PSO J011+09	00:45:33.57	+09:01:56.9	2021-07-15	81.00	45.36	58.97	48.78
0884992001	PSO J036.5+03.0	02:26:01.88	+03:02:59.4	2021-07-19	85.00	47.56	68.69	57.24
0884991701	PSO J231.6−20.8	15:26:37.83	−20:50:00.7	2021-07-29	109.00	67.07	90.45	79.05
0884991501	VDES J0244−5008	02:44:01.02	−50:08:53.7	2021-08-04	89.00	67.23	82.87	73.48
0884993801	ULAS J1342+0928	13:42:08.10	+09:28:38.6	2021-12-24	102.00	46.53	55.36	54.09
0884991101	VDES J0020−3653	00:20:31.47	−36:53:41.8	2022-01-01	87.00	36.54	64.67	61.26
0884992901	ATLAS J029−36	01:59:57.97	−36:33:56.6	2022-01-03	85.00	55.65	71.49	65.45
0886201201	J1007+2115	10:07:58.26	+21:15:29.2	2022-05-28	83.40	51.37	67.37	66.06
0886210301	VHS J0411−0907	04:11:28.62	−09:07:49.7	2022-07-31	95.05	53.12	81.62	78.07
0886210801	PSO J231.6−20.8	15:26:37.83	−20:50:00.7	2022-08-14	103.00	52.19	78.10	36.97
0886220301	SDSS J1148+5251	11:48:16.64	+52:51:50.2	2022-11-08	86.70	55.77	68.70	67.78
0886210201	VDES J0020−3653	00:20:31.46	−36:53:41.8	2022-11-16	87.20	36.90	49.05	48.24
0886220201	PSO J011+09	00:45:33.56	+09:01:56.9	2023-01-13	88.00	50.97	69.09	68.32
0884990901	DES J0252−0503	02:52:16.64	−05:03:31.8	2023-01-15	87.50	27.68	35.85	36.72
0886220701	CFHQS J0050+3445	00:50:06.67	+34:45:22.6	2023-02-01	34.90	4.78	12.21	12.04
0886200201	J1007+2115	10:07:58.26	+21:15:29.2	2023-05-14	83.80	56.89	68.05	66.32
0886221501	PSO J011+09	00:45:33.56	+09:01:56.9	2023-07-01	85.10	44.98	62.28	47.18
0886221401	ATLAS J025−33	01:42:43.69	−33:27:45.6	2023-07-19	94.85	43.63	81.28	60.77
0886201001	DES J0252−0503	02:52:16.64	−05:03:31.8	2023-07-25	89.50	37.08	50.80	49.31
0886200901	DES J0252−0503	02:52:16.64	−05:03:31.8	2023-07-29	83.00	68.97	80.17	78.16
0886210901	PSO J231.6−20.8	15:26:37.83	−20:50:00.7	2023-07-31	86.30	36.97	59.94	58.47
Non-HYPERION QSOs								
0803161101	PSO J159−02	10:36:54.19	−02:32:37.94	2017-12-22	23.00	16.97	20.87	19.81
0148560501	SDSS J1030+0524	10:30:27.11	+05:24:55.06	2003-05-22	103.88	51.99	64.90	66.54

Notes. We report the observations of the HYPERION QSOs from the archive and from the *XMM-Newton* Multi-Year Heritage X-ray programme, up to August 2023, we included also the most recent *XMM-Newton* data of the HYPERION source ATLAS J029−36 (OBSID 0930591101 and 0930591201, P.I. Norbert Schartel) and archival *XMM-Newton* observations of the non-HYPERION QSOs.

2011; Coatman et al. 2016; Reed et al. 2019; Travascio et al. 2020; Yang et al. 2021) and/or the peak of a Gaussian or multi-Gaussian profile (e.g. De Rosa et al. 2014; Mazzucchelli et al. 2017; Vietri et al. 2018; Shen et al. 2019; Meyer et al. 2019; Schindler et al. 2020; Wang et al. 2021a; Mazzucchelli et al. 2023). These different $v_{\rm C\,IV}$ definitions, coupled with different fitting approaches for the line modelling involving one or more Gaussians (depending on the signal-to-noise ratio and the resolving power of the analysed spectra) and the pseudo-continuum models of Fe II templates, result in a range of different C IV velocity shift values, even for the same source, that differ by up to a factor of 2 (see e.g. ULAS J1120+0641 and PSO J231.6-20.8). We show in Table 3 all the values of the C IV velocity shift and its rest-frame equivalent width ($\rm REW_{C\,IV}$) reported in the literature to date for each QSO considered in this work. The $\rm REW_{C\,IV}$ of the QSOs belonging to the ESO Large Programme XQR-30 were calculated using the same approach of Mazzucchelli et al. (2023); details will be reported in Bischetti et al. (in prep.). For the analysis performed in this work we took into account multiple values of $v_{\rm C\,IV}$ and/or $\rm REW_{C\,IV}$ (as explained in Section 3.2).

3. Analysis

3.1. Spectral analysis

The spectral analysis was performed using the `xspec` v.12.12.1 software package (Arnaud 1996). Following Zappacosta et al. (2023), we performed the modelling by using the Cash statistics with direct background subtraction (W-stat in `xspec`, Cash 1979; Wachter et al. 1979). We adopted a simple power law model, modified by Galactic absorption only, and included a constant in the model to take into account the possible flux variations of the sources within observations taken at different epochs (parametrized by `const*tbabs*zpowerlaw` in `xspec`)[1]. For the Galactic column density at the position of the sources, we adopted HI4PI Collaboration 2016 maps. The analysis was performed over the optimized 0.3–7 keV energy range (see Appendix C in Zappacosta et al. 2023) which corresponds to a

[1] We choose to use a simple power-law model absorbed just by the Galactic column density since all the targets are type 1 sources. Moreover, Zappacosta et al. (2023) verified that the absorption in these QSOs is $N_{\rm H} < 10^{21-22}\,{\rm cm^{-2}}$ and, given their high-z, the resulting rest-frame region of the spectrum is not sensitive to such column densities.

Table 3. Values of $v_{\rm C\,IV}$ and $\rm REW_{C\,IV}$ reported in literature for the sources in our sample.

Target	$v_{\rm C\,IV}$ [km s^{-1}]	$\rm REW_{C\,IV}$ [Å]	Ref.	Target	$v_{\rm C\,IV}$ [km s^{-1}]	$\rm REW_{C\,IV}$ [Å]	Ref.
ULAS J1342+0928	−5986	–	1	PSO J036.5+03.0	−5386 ± 689	41.5 ± 1.1	6
	−4935 ± 758	12.90 ± 1.40	2		−4382	–	1
	−5978 ± 889	–	3		−4382	–	1
	–	21.18 ± 0.69	4		−3727 ± 135	$21.83^{+0.80}_{-1.10}$	9, 12
J1007+2115	−3183 ± 1475	10.00 ± 1.60	2	ATLAS J025-33	−2461 ± 251	$18.82^{+1.50}_{-1.20}$	9, 12
	−3220 ± 362	–	5		−4032 ± 340	–	11
DES J0252−0503	−4618 ± 762	17.30 ± 1.00	2	ATLAS J029-36	−1924 ± 377	$14.59^{+1.90}_{-0.50}$	9, 12
	−4090	–	7		−2433 ± 158	-	11
VDES J0020−3653	−1700 ± 100	55.00 ± 1.00	8	VDES J0244-5008	−3200 ± 310	24.00 ± 2.00	8
PSO J231.6−20.8	−5131	–	1	VDES J0224-4711	−2000 ± 160	44.00 ± 2.00	8
	−2528 ± 116	$6.66^{+2.00}_{-1.30}$	9, 12		−1634 ± 56	-	3
	−5861 ± 318	23 ± 1.2	6		−1808 ± 42	$56.50^{+1.70}_{-1.80}$	9, 12
PSO J011+09	−3356 ± 338	7.38 ± 1.75	4	SDSS J1148+5251	−2803 ± 51	44.68 ± 2.46	10
SDSS J0100+2802	−2496 ± 316	5.11 ± 0.50	9, 12	CFHQS J0050+3445	864 ± 487	63.68 ± 2.60	10
PSO J159−02	−726 ± 120	54.70 ± 3.82	4	PSO J308−21	−2003 ± 233	33.15 ± 1.61	4
SDSS J1030+0524	−822	–	1	SDSSJ 1306+0356	−855	–	1
	−768 ± 379	32.77 ± 2.37	4		−735 ± 33	47.89 ± 1.76	4
	−1092 ± 92	–	9		−769 ± 189	–	9
ULAS J1120+0641	−2602 ± 285	–	6	SDSS J1602+4228	−311 ± 479	56.19 ± 3.23	10
	−2966	–	1				
	−2007 ± 133	25.90 ± 2.40	2				
	−2520 ± 199	–	3				
	−1583 ± 115	33.10 ± 1.00	4				

Notes. (1) Meyer et al. (2019); (2) Yang et al. (2021); (3) Wang et al. (2021a); (4) Farina et al. (2022);(5) Yang et al. (2020); (6) Mazzucchelli et al. (2017); (7) Wang et al. (2020); (8) Reed et al. (2019); (9) Mazzucchelli et al. (2023); (10) Shen et al. (2019); (11) Chehade et al. (2018); (12) Bischetti et al. (in prep.).

rest-frame energy band spanning from ∼2 keV to ∼50 keV, modelling the EPIC-pn together with the two EPIC-MOS camera and leaving as free parameters Γ and the normalization.

The analysis of the observations performed during the first year of the *XMM-Newton* Multi-Year Heritage programme are presented in Zappacosta et al. (2023). We have included these data in the current spectral analysis. No flux and/or spectral variations have been detected in the sources that have observations during multiple epochs. The values obtained from the spectral analysis are reported in Table 4, together with the same parameters taken from the literature for all the sources that were not analysed for this work (i.e. SDSS J1602+4228, SDSSJ1306+0356, PSO J308-21; see Ref. column in Table 4).

The most remarkable result arising from the spectral analysis of our sample of $z > 6$ QSOs is the steep shape of their X-ray spectra (as previously reported by Zappacosta et al. 2023). The derived steep X-ray continuum slopes might be, partly or entirely, associated with a particularly low $E_{\rm cut}$, well below 50 keV. In the presence of limited quality spectra such as those we are reporting for $z > 6$ QSOs, steep X-ray continuum slopes can be obtained by either steep Γ power laws or by canonical Γ power laws (e.g. Γ = 1.9) with a high-energy cut-off $E_{\rm cut} < 20$ keV. Hence, we tested the latter hypothesis on the sources in our sample for which we have *XMM-Newton* data, by modelling their spectra with a cut-off power law model (`const*tbabs*zcutoffpl` in `xspec`), fixing the photon index to Γ = 1.9. We were able to measure the cut-off value for only the 50% of the spectra; we found lower limits for the others (see Table 4).

Steep Γ and $E_{\rm cut} < 20$ keV are both tracers of relatively cold coronae. The fact that we found generally steep continuum slopes could indicate low coronal temperatures. Our data does not allow us to discriminate between a simple power–law model or a cut-off power-law model, and thus for the following correlation analysis we use the better constrained Γ to characterize the X-ray continuum.

3.2. Correlation analysis

We checked the relations between the coronal X-ray properties, the velocities of the AD winds and other parameters regarding the physics of the AD and the growth of the SMBH of the QSOs in our sample. The parameters related to the coronal properties used in this analysis are Γ and $L_{\rm x}$. As tracers of the AD winds, we used $v_{\rm C\,IV}$ and $\rm REW_{C\,IV}$. We also tested the relation of the coronal X-ray properties with some physical properties of the QSOs in the sample, such as $L_{\rm bol}$, $\lambda_{\rm Edd}$ and $M_{\rm BH}$. For the SMBH growth properties the redshift, z, and $M_{\rm s,Edd}$ are used.

The presence of a possible relation between two quantities was investigated by using the `linmix` code, a hierarchical Bayesian model for fitting a straight line to data with errors in the x and the y directions (Kelly 2007). To perform the fitting we used a linear model to the data using the relation

$$y = Ax + B \quad (2)$$

where x is the independent variable.

Table 4. Best-fit parameters from the X-ray spectral analysis.

Target	Γ	W-stat/d.o.f.	E_{cut} [a] [keV]	W-stat/d.o.f.	log(L_x) [b] [erg s^{-1}]	Net counts	Ref.
HYPERION QSOs: *XMM-Newton* Heritage programme							
ULAS J1342+0928	$2.93^{+0.43}_{-0.37}$	393/319	8.5^{+40}_{-5}	393/319	45.22 ± 0.08	123 (†)	1
J1007+2115	$2.66^{+0.78}_{-0.78}$	325/309	14.8^{+15}_{-10}	324/309	44.50 ± 0.09	42 (†)	1
ULAS J1120+0641	$2.65^{+0.35}_{-0.32}$	148/155	7.5^{+20}_{-4}	148/155	45.39 ± 0.06	75 (†)	1
DES J0252-0503	$2.63^{+0.92}_{-0.92}$	368/347	3.9^{+30}_{-2}	369/347	45.08 ± 0.05	55 (†)	1
VDES J0020-3653	$2.73^{+0.45}_{-0.32}$	273/305	9.2^{+25}_{-5}	273/305	45.12 ± 0.08	80 (†)	1
VHS J0411-0907	$1.84^{+0.48}_{-0.48}$	192/159	>50	193/159	45.13 ± 0.05	134 (†)	1
VDES J0244-5008	$2.35^{+0.30}_{-0.25}$	298/309	>25	298/309	45.28 ± 0.04	124 (†)	1
PSO J231.6-20.8	$2.30^{+0.62}_{-0.67}$	918/841	>13	918/841	45.09 ± 0.09	170 (†)	1
PSO J036.5+03.0	$3.05^{+1.10}_{-0.85}$	64/60	10.5^{+50}_{-5}	65/60	44.95 ± 0.11	52 (†)	1
VDES J0224-4711	$2.08^{+0.20}_{-0.20}$	181/153	>28	182/153	45.58 ± 0.05	97 (†)	1
PSO J011+09	$2.58^{+0.82}_{-0.82}$	340/310	>13	339/310	45.04 ± 0.11	91 (†)	1
SDSS J1148+5251	$2.38^{+0.39}_{-0.39}$	168/157	16.4^{+60}_{-8}	168/157	45.18 ± 0.08	153 (†)	1
SDSS J0100+2802	$2.41^{+0.15}_{-0.09}$	160/165	31.0^{+53}_{-13}	160/165	45.76 ± 0.03	290 (†)	1
ATLAS J025-33	$2.03^{+0.42}_{-0.37}$	166/156	>20	165/156	45.24 ± 0.03	182 (†)	1
CFHQS J0050+3445	$2.02^{+0.43}_{-0.41}$	198/191	>50	198/191	45.07 ± 0.08	80 (†)	1
ATLAS J029-36	$2.54^{+0.24}_{-0.21}$	492/475	34^{+13}_{-10}	492/475	44.91 ± 0.08	259 (†)	1
Non-HYPERION QSOs							
PSO J159−02	$1.86^{+0.45}_{-0.40}$	139/155	>23	139/155	45.41 ± 0.11	90 (†)	1
SDSS J1030+0524	$2.19^{+0.20}_{-0.19}$	183/165	29^{+58}_{-13}	182/165	45.59 ± 0.09	207 (†)	1
PSO J308−21	$2.39^{+0.36}_{-0.37}$	–	–	–	45.36 ± 0.15	72 (⋆)	3
SDSS J1602+4228	$2.19^{+0.74}_{-0.71}$	–	–	–	45.56 ± 0.08	30 (⋆)	2
SDSS J1306+0356	$1.83^{+0.26}_{-0.25}$	–	–	–	45.23 ± 0.05	133 (⋆)	2

Notes. [a]This cut-off value is obtained when applying the `zcutoffpl` model in `xspec` with Γ fixed to a value of 1.9. [b]L_x is measured in the 2–10 keV rest-frame energy band. (†)Sum of the EPIC-pn, EPIC-MOS1 and EPIC-MOS2 net counts in the 0.3–7 keV energy range. (⋆)*Chandra* total net counts in the 0.5–7 keV energy range. (1) This work; (2) Vito et al. (2019); (3) Connor et al. (2019).

For more than half of the sample sources, multiple values of $v_{C\,IV}$ and/or $REW_{C\,IV}$ are reported in the literature, often measured with different methods (see Section 2.3). To take this into account, we iterated the fitting process 10 000 times, each time randomly choosing one value to consider among those available for the QSOs showing more than one $v_{C\,IV}$/$REW_{C\,IV}$ value. The final values of slope, intercept (with relative uncertainties), correlation coefficient and null hypothesis probabilities are the mean among all the values of the fits within $\pm1\sigma$ from the peak of the χ^2 distribution.

Table 5 reports the best-fit slopes and intercepts along with the significance of the correlation analysis and correlation coefficients for the relations investigated in this work.

4. Results

Among the relations involving X-ray parameters, we found a significant ($>3\sigma$) relation between Γ and $v_{C\,IV}$ (see Figure 1). To compute this relation we used the method explained in Section 3.2, which allowed us to take into account all the different values of $v_{C\,IV}$ reported in the literature (see also Section 2.3). We checked the presence of the Γ−λ_{Edd} relation in the QSOs in our sample but we did not find any significant correlation (see Table 5 and upper left panel of Figure 2).

Following the results presented in Zappacosta et al. (2020), we verified the presence of a relation between $v_{C\,IV}$ and L_x. We performed this analysis on the sources with similar L_{bol} (within 0.5 dex), removing the obvious outlier of SDSS J0100+2802 that exhibits a L_{bol} much larger than other QSOs in the sample. We found a mild relation ($\sim1.5\sigma$) between $v_{C\,IV}$ and L_x for the presented sample of $z > 6$ QSOs. However, the trend is consistent, within the errors, with what was found by Zappacosta et al. (2020) (see upper right panel of Figure 2 and Table 5).

In light of the marginal evidence ($\sim2.2\sigma$) for a dependence between $M_{s,Edd}$ and Γ reported in Zappacosta et al. (2023), we tested whether it could be potentially associated with an evolutionary phenomenon or with the particularly fast SMBH mass growth of these sources. Thus, we investigated for a possible relation between Γ, $M_{s,Edd}$ and z. We identified moderate log($M_{s,Edd}$)−Γ (2.5σ) and z−Γ (2.3σ) relations (see lower left and lower right panels of Figure 2 respectively, and Table 5).

A significant relation ($>3\sigma$) is also found between $REW_{C\,IV}$ and $v_{C\,IV}$ (see Figure 3). This trend is already well established in QSOs (Richards et al. 2011; Hamann et al. 2017; Vietri et al. 2018, 2020; Temple et al. 2021; Schindler et al. 2020; Matthews et al. 2023). Assuming the C IV line profile is the result of the combination of a standard peaked virialized component and an outflowing shallower component, it is observed that, as the wind velocity increases, the standard virialized component of the line profile decreases.

Other tested relations are also reported in Table 5, where we list the best-fitting parameters. The plots are reported in

Table 5. Best-fit linear relations ($y = Ax + B$) tested in this work, together with their correlation coefficients, null-hypothesis probabilities referred to the goodness of the fit and statistical significance.

Relation (y vs. x)			Slope (A)	Intercept (B)	Pearson	$1 - P_{\rm null}$	σ
Γ	vs.	$v_{\rm C\,IV}$	$(-1.72 \pm 0.79) \times 10^{-4}$	1.93 ± 0.19	-0.901	0.9992	3.2
Γ	vs.	$\log(M_{\rm s,Edd})$	$(3.87 \pm 1.89) \times 10^{-1}$	0.96 ± 0.65	0.554	0.9944	2.5
Γ	vs.	$\log(REW_{\rm C\,IV})$	$(-3.66 \pm 2.75) \times 10^{-1}$	2.79 ± 0.40	-0.760	0.9825	2.4
Γ	vs.	z	$(4.62 \pm 2.58) \times 10^{-1}$	-0.71 ± 1.67	0.813	0.9794	2.3
Γ	vs.	$\log(L_{\rm x})$	$(-1.10 \pm 4.07) \times 10^{-1}$	7.30 ± 1.84	-0.147	0.7506	1.1
Γ	vs.	$\log(\lambda_{\rm Edd})$	$(2.94 \pm 4.23) \times 10^{-1}$	2.31 ± 0.10	0.426	0.6287	<1
Γ	vs.	$\log(M_{\rm BH})$	$(4.57 \pm 4.13) \times 10^{-2}$	1.85 ± 3.88	0.087	0.4305	<1
Γ	vs.	$\log(L_{\rm bol})$	$(1.05 \pm 2.87) \times 10^{-2}$	-2.71 ± 1.47	0.172	0.0919	<1
$\log(L_{\rm x})$	vs.	z	$(-2.48 \pm 1.52) \times 10^{-1}$	46.86 ± 1.12	-0.403	0.8611	1.5
$\log(L_{\rm x})$	vs.	$v_{\rm C\,IV}$	$(6.90 \pm 4.53) \times 10^{-5}$	45.36 ± 0.12	0.436	0.8534	1.5
$\log(L_{\rm x})$	vs.	$\log(M_{\rm BH})$	$(1.44 \pm 2.78) \times 10^{-1}$	43.88 ± 2.60	0.157	0.8345	1.5
$\log(L_{\rm x})$	vs.	$\log(REW_{\rm C\,IV})$	$(1.74 \pm 2.18) \times 10^{-1}$	44.98 ± 0.31	0.263	0.8144	1.4
$\log(L_{\rm x})$	vs.	$\log(M_{\rm s,Edd})$	$(-1.74 \pm 1.31) \times 10^{-1}$	45.83 ± 0.86	-0.350	0.7874	1.3
$\log(L_{\rm x})$	vs.	$\log(L_{\rm bol})$	$(413 \pm 2.60) \times 10^{-1}$	25.67 ± 12.32	0.395	0.7076	1.1
$\log(L_{\rm x})$	vs.	$\log(\lambda_{\rm Edd})$	$(1.50 \pm 2.93) \times 10^{-1}$	45.25 ± 0.08	0.142	0.0806	<1
$\log(REW_{\rm C\,IV})$	vs.	$v_{\rm C\,IV}$	$(1.58 \pm 0.47) \times 10^{-4}$	1.77 ± 0.13	0.786	0.9999	3.7
$v_{\rm C\,IV}$	vs.	$\log(M_{\rm s,Edd})$	$(-1.64 \pm 6.43) \times 10^{+2}$	$(3.30 \pm 2.23) \times 10^{+3}$	-0.603	0.9934	2.5
$\log(M_{\rm s,Edd})$	vs.	z	(1.06 ± 0.15)	-3.50 ± 1.02	0.867	0.9999	3.7
$v_{\rm C\,IV}$	vs.	z	$(-2.03 \pm 0.78) \times 10^{+3}$	$(1.09 \pm 0.51) \times 10^{+4}$	-0.613	0.9962	2.7

Notes. The most relevant relations are discussed in Section 5.

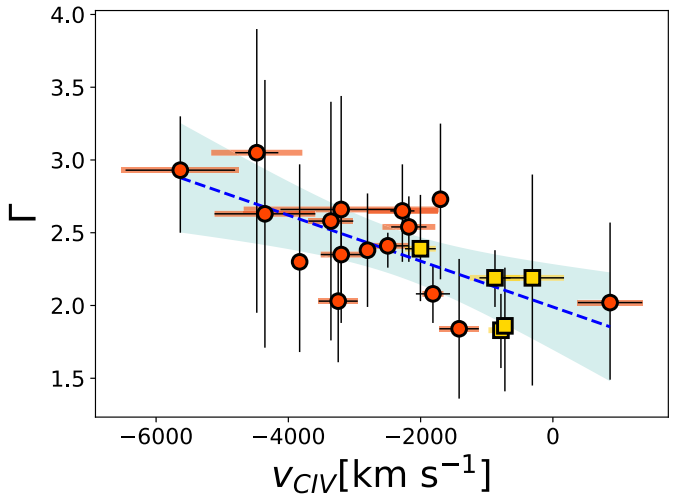

Fig. 1. Plot of Γ vs. $v_{\rm C\,IV}$. The orange circles and the yellow squares represent the HYPERION and non-HYPERION QSOs, respectively. For simplicity we report in the plot the mean values of $v_{\rm C\,IV}$ (see Table 1), but the fit takes into account all the existing values of $v_{\rm C\,IV}$ (see Section 3.2). The thick coloured errorbars represent the maximum deviation from the mean, while the thin black errorbars represent the mean error. The dashed blue line is the linear regression while the shaded region represents the combined 1σ error on the slope and normalization (see Table 5). This is valid for all the following plots.

Figure 4. Among these other tested relations, we note that a relation is found between $\rm REW_{C\,IV}$ and Γ with a significance of $\sim 2\sigma$ but this is a by-product of the $v_{\rm C\,IV}$–Γ and $v_{\rm C\,IV}$–$REW_{\rm C\,IV}$ relations. Moreover, we report a significant ($>3\sigma$) $M_{\rm s,Edd}$–z relation (see Table 5); however, it is due to the definition of $M_{\rm s,Edd}$ (see Eq. (1)) where there is a time (i.e. redshift) dependence.

5. Discussion

5.1. Linking X-ray corona and accretion disc winds

We investigated the relation between the X-ray photon index and the velocities of the rest-frame UV disc winds in our sample of $L_{\rm bol} > 10^{47}$ erg s^{-1}, $z > 6$ QSOs and we discovered that they are related: the steeper the X-ray spectrum, the faster the C IV winds.

The interpretation of this measured relation is not straightforward but its presence may suggest a physical link between the disc-corona system and the terminal velocities of the AD winds. Current models of the AD wind and X-ray coronae for highly-accreting AGN (e.g. Kubota & Done 2018; Ni et al. 2018; Jin et al. 2023), assuming innermost hotter corona and outer AD configuration, can provide a qualitative explanation of how the Γ–$v_{\rm C\,IV}$ relation may originate. In this configuration, the physical properties and the relative geometry of the AD-corona system could play a crucial role in reproducing the Γ–$v_{\rm C\,IV}$ relation. In the case of a sufficiently high dimensionless mass accretion rate (ratio of the accretion rate, $\dot{M}$, to the Eddington accretion rate, $\dot{m} = \dot{M}/\dot{M}_{\rm Edd}$ where $\dot{M}_{\rm Edd} = L_{\rm Edd}/\eta c^2$), it has been suggested in different works (e.g. Luo et al. 2015; Sądowski & Narayan 2016; Kubota & Done 2019; Jiang et al. 2019a) that the inner part of a standard optically thick geometrically thin AD (Shakura & Sunyaev 1973) puffs up (i.e. slim disc, Czerny 2019), due to the high radiation-pressure of UV photons. The inner puffed-up part of the AD increases the EUV/soft X-ray flux seen by the corona (see Figure 5a), leading to a much more efficient cooling of the corona and a steeper X-ray spectrum. Furthermore, a similar inner puffed-up component of the AD shields the standard part of the AD beyond it from the X-rays. This prevents significant over-ionization and allows the line-driven acceleration of C IV-emitting gas from the more internal regions of the thin AD, leading to winds with higher velocities. Conversely, for lower accretion rates, the absent or reduced puffing of the inner part of the AD results in fewer UV-seed

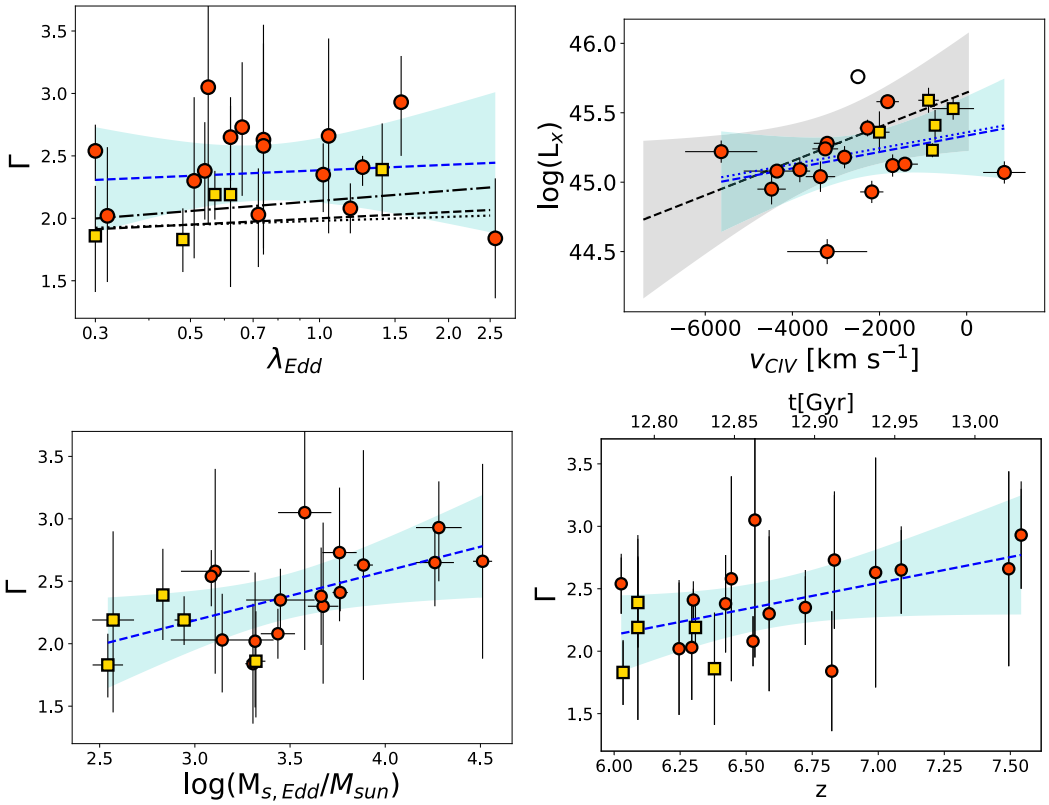

Fig. 2. Plots of some of the correlations tested for this work. Upper left panel: Γ vs. log(λ_{Edd}). We report for comparison the linear relations from Trakhtenbrot et al. 2017 (black dashed line), Liu et al. 2021 (black dot-dashed line) and Tortosa et al. 2023 (black dotted line); Upper right panel: $v_{C\,IV}$ vs. L_x, we also report the linear relation (black dashed line) and the combined 1σ error on the slope and normalization (grey shaded region) from Zappacosta et al. (2020). The empty dot is SDSS J0100+2802, which is not included in the fitting process given its different value of L_{bol} (see Section 5.2). The blue dotted line is the linear relation when including SDSS J0100+2802. We also report the linear relation from Zappacosta et al. 2020 (black dotted line). The $v_{C\,IV}$ values plotted here are, for simplicity, the mean values derived using all the available values reported in Table 3. We note that the fit takes into account all the existing values of $v_{C\,IV}$ (see Section 3.2); Lower left panel: Γ vs. log($M_{s,Edd}$); Lower right panel: Γ vs. z.

photons. Consequently, the corona cooling is lower and the outcoming X-ray continuum slope is flatter, but consistent with most AGN (see Figure 5b). Accordingly, the harder ionizing X-ray radiation from the corona will not be shielded, over-ionizing the inner regions of the AD. Therefore, the winds will be launched at larger radii, with slower velocity.

According to this scenario, we would expect, together with the measured Γ−$v_{C\,IV}$ relation, a Γ−λ_{Edd} relation; however, we do not recover it (see Section 5.2).

The properties of our sample resemble those of the narrow-line Seyfert 1 galaxies (NLS1s; Mineshige et al. 1994; Collin et al. 2002; Collin & Kawaguchi 2004), although scaled up in mass and luminosity by at least two orders of magnitude. Actually, NLS1s host SMBHs accreting close to or above the Eddington limit (Pounds et al. 1995; Komossa et al. 2006; Jin et al. 2016, 2017; Berton et al. 2015). They show very steep X-ray continuum slopes, possibly driven by enhanced EUV/soft X-ray emission (Boller et al. 1996; Brandt et al. 1997; Leighly 1999a,b) and high-velocity blueshifted C IV lines (Sulentic et al. 2000, 2002; Wills et al. 2000; Leighly & Moore 2004). The QSOs within our sample typically exhibit X-ray continuum slopes that are steeper compared to analogous QSOs at redshifts below 6 (but see e.g. the case of PHL 1092, Miniutti et al. 2009, 2012). Focusing on similar M_{BH} and L_{bol} ranges, the population of X-ray unabsorbed weak emission-line quasars (WLQ; e.g. Fan et al. 1999; Diamond-Stanic et al. 2009; Plotkin et al. 2010) show steep X-ray spectra (Luo et al. 2015) and

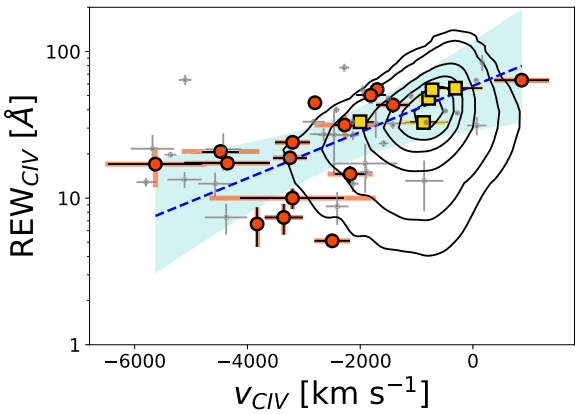

Fig. 3. The REW$_{C\,IV}$ vs. $v_{C\,IV}$ relation compared with the 0.05, 0.1, 0.3, 0.5, 0.68, 0.9 and 0.99 contour levels (relative to the peak) of the SDSS DR7 sample (Shen et al. 2011; Vietri et al. 2018) and with the values from Schindler et al. 2020 (grey points). For simplicity, we plot here the mean values derived using all the available values reported in Table 3. We note that the fit takes into account all the existing values of $v_{C\,IV}$ and REW$_{C\,IV}$(see Section 3.2).

velocity shifts of the C IV, $v_{C\,IV}$ ∼ 1000−8000 km/s (Wu et al. 2011, 2012; Luo et al. 2015). Despite the similarities, to our knowledge, to date no evidence of a relation between Γ and $v_{C\,IV}$

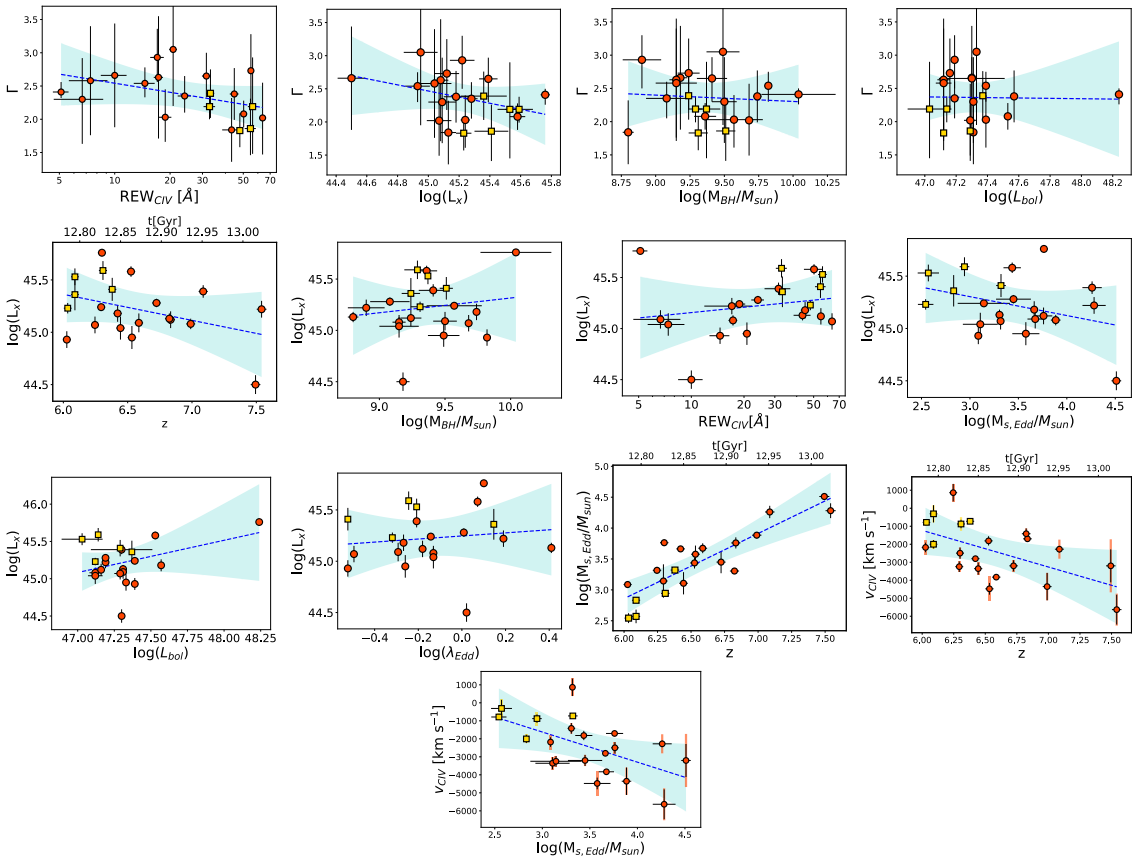

Fig. 4. From top to bottom and from left to right, we report: Γ vs. REW$_{\rm C\,IV}$; Γ vs. log($L_{\rm x}$); Γ vs. log($M_{\rm BH}$); Γ vs. log($L_{\rm bol}$); log($L_{\rm x}$) vs. z; log($L_{\rm x}$) vs. log($M_{\rm BH}$); log($L_{\rm x}$) vs. REW$_{\rm C\,IV}$; log($L_{\rm x}$) vs. log($M_{\rm s,Edd}$); log($L_{\rm x}$) vs. log($L_{\rm bol}$); log($L_{\rm x}$) vs. Γ; log($L_{\rm x}$) vs. log($\lambda_{\rm Edd}$); log($M_{\rm s,Edd}$) vs. z; $v_{\rm C\,IV}$ vs. z; $v_{\rm C\,IV}$ vs. log($M_{\rm s,Edd}$).

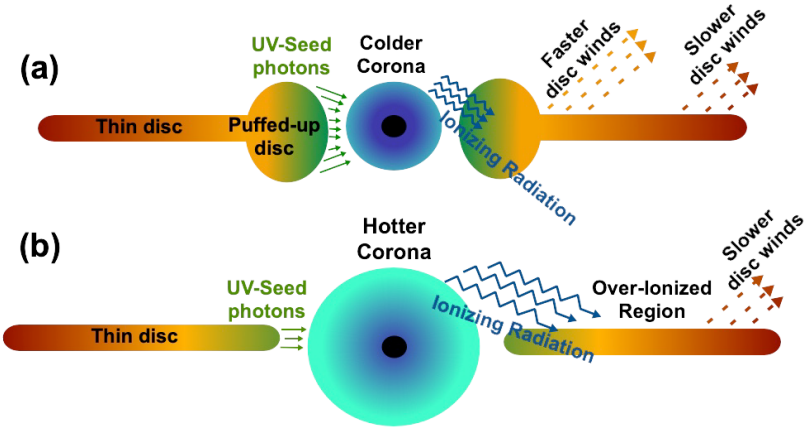

Fig. 5. Scheme of the geometry of the AD-corona model proposed to provide a qualitative explanation for the observed Γ−$v_{\rm C\,IV}$ relation. Panel (a): AD-corona system in which the inner part of the AD is puffed up and the X-ray corona is cold, producing steep X-ray spectrum. In this configuration, faster AD winds can be launched from more internal AD regions. Panel (b): standard AD and a hotter X-ray corona producing a canonical X-ray spectrum where only low-velocity winds can be launched from outer regions of the disc.

has been reported for these categories of objects, nor for the population of AGN in general.

The relation between the X-ray continuum slope and the AD wind velocity has never been reported for AGN at $z < 6$. In Zappacosta et al. (2020), the Γ vs. $v_{\rm C\,IV}$ relation was tested for a sample of $z \sim 2$–4 WISE/SDSS-selected Hyper-luminous QSOs (WISSH), but no correlation was recovered. In Figure 6 we report the Γ vs. $v_{\rm C\,IV}$ relation for the Zappacosta et al. (2020) sample and the sample of $z \simeq 3.0$–3.3 QSOs selected from the Sloan Digital Sky Survey (SDSS) seventh Data Release (DR7) (Nardini et al. 2019; Lusso et al. 2021), along with our sample. We performed a correlation analysis over the combined sample of QSOs at $z < 6$ using the same method described in Section 3.2, but we do not find a significant relation (<1σ and Pearson correlation coefficient $\rho = 0.162$). The absence of a similar relation for QSOs with similar $L_{\rm bol}$ ($\gtrsim 10^{47}$ erg s^{-1}) and $\lambda_{\rm Edd}$ at $z < 6$, may be driven by a different $\dot{m}$. In particular, at a given $\lambda_{\rm Edd}$, the $z < 6$ QSOs may have a more standard AD-corona configuration (see Figure 5b) than $z > 6$ QSOs, as a consequence of lower $\dot{m}$. This would imply higher radiative efficiencies and consequently higher BH spins at $z < 6$. Thus, the measured Γ vs. $v_{\rm C\,IV}$ relation may be a distinctive feature of $z > 6$ QSOs, possibly indicating specific high $\dot{m}$ regimes ranging between the disc-corona configurations sketched in Figure 5.

Within our sample (see Figure 1), the HYPERION sources contribute with steeper X-ray spectra and faster and more power-

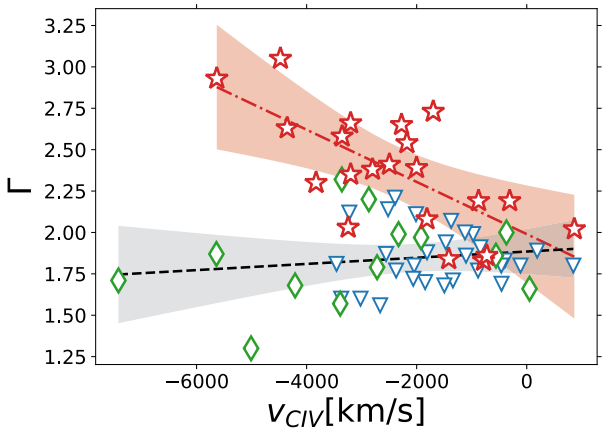

Fig. 6. Γ vs. $v_{\rm C\,IV}$ for our sample of $z > 6$ QSOs (red stars) compared with a sample of luminous QSOs at $z < 6$: the WISSH QSOs at $z = 2-4$ (Zappacosta et al. 2020) (green diamonds) and blue QSO at $z \simeq 3.0-3.3$ (Nardini et al. 2019; Lusso et al. 2021) (blue inverted triangles). We report the linear relations we found for our sample of QSOs at $z > 6$ (red dot-dashed line) and for the combined sample of lower z QSOs (black dashed line). The shaded regions represent the combined 1σ error on the slope and normalization.

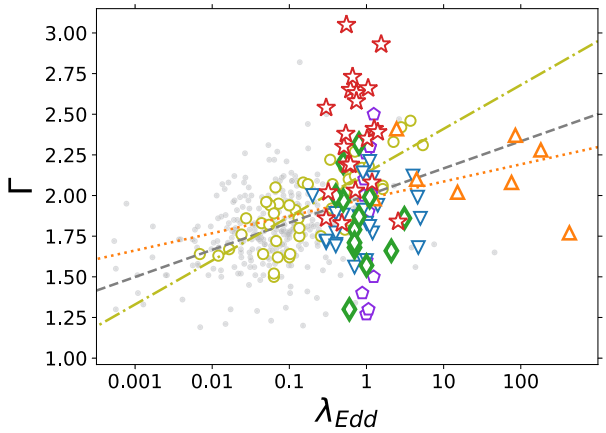

Fig. 7. Γ vs. $\lambda_{\rm Edd}$ for our sample of $z > 6$ QSOs (red stars) compared with the WISSH sample of QSOs at $z = 2-4$ (green diamonds, Zappacosta et al. 2020), the SDSS DR7 blue QSOs at $z \simeq 3.0-3.3$ (blue inverted triangles, Trefoloni et al. 2023), local hyper-Eddington AGN (orange triangles, Tortosa et al. 2023), radio-quiet super-Eddington accreting QSOs at $0.4 \leq z \leq 0.75$ (purple, pentagons Laurenti et al. 2022), a sample of $z < 0.4$ AGN (yellow circles, Liu et al. 2021) and the local type 1 AGN belonging to the BASS sample (grey points, Trakhtenbrot et al. 2017; Ricci et al. 2017). We also report the linear relations from Trakhtenbrot et al. 2017 (grey dashed line), Liu et al. 2021 (yellow dot-dashed line) and Tortosa et al. 2023 (orange dotted line).

ful winds (i.e. with higher kinetic power, $\propto v^3_{\rm C\,IV}$; e.g. Vietri et al. 2018), driving the observed relation. This suggests that the HYPERION selection, based on $M_{\rm s,Edd}$ and $L_{\rm bol}$, allows us to select the most extreme QSOs in terms of Γ and AD winds (see Section 5.3). We calculated the average $v_{\rm C\,IV}$ for the Yang et al. 2021 ($z > 6.3$) and Farina et al. 2022 ($z > 6.0$) QSOs samples (avoiding duplication with the HYPERION sources), finding ∼−1540 km/s and ∼−1700 km/s, respectively. Matching the HYPERION sample to the same redshift ranges of Yang et al. (2021) and Farina et al. (2022), we found an average $v_{\rm C\,IV} \sim -3100$ km/s and ∼−2800 km/s, respectively. Interestingly, the low $\Gamma = 1.83$, resulting from the stacking spectral analysis of Nanni et al. (2017) for ten QSOs with $5.7 < z < 6.1$, may be explained according to our reported relation if the sources employed in their stacking analysis had, on average, a very low $v_{\rm C\,IV}$ (from our relation we would expect ∼600 km/s, see Figure 1).

5.2. Testing the presence of an accretion rate and X-ray radiative power dependence

We analysed the possible presence of a relation between $\lambda_{\rm Edd}$ and Γ in the QSOs in our sample. The analysed sample of QSOs covers a limited range size for $\lambda_{\rm Edd}$, with a limited number of $z > 6$ sources showing a large dispersion in terms of Γ. It should be considered that there are large uncertainties on the measure of $\lambda_{\rm Edd}$ (related to the measure of $M_{\rm BH}$). Moreover, while in sub-Eddington regimes $L_{\rm bol} \propto \dot{m}$, at higher accretion rates this is not true anymore, since their relation is strongly affected by the radiative efficiency of the accretion, also related to the spin of the SMBH (Czerny 2019; Sadowski 2011; Madau et al. 2014). In particular, in the slim disc (puffed-up disc) scenario, $\dot{m}$ saturates due to photon trapping and advection, which cause a decrease in the radiative efficiency. Because the radiative efficiency is dependent on the spin of the SMBH, for higher SMBH spin, $\dot{m}$ saturates more (see Fig. 1 of Madau et al. 2014). In our sample we analysed a very narrow range of $\lambda_{\rm Edd}$ which is also in the region of the transition between the standard geometrically thin disc and the geometrically thick disc (slim disc). In this situation $\lambda_{\rm Edd}$ may not be a good proxy for $\dot{m}$ and this could be another reason why we do not see a $\Gamma-\lambda_{\rm Edd}$ relation. All these prevented us from obtaining firm constraints on the presence of a possible relation between the two quantities. However, we can compare this result and the distribution of HYPERION sources in this parameter space with that reported for samples of lower-z objects reported in the literature.

We compared the Γ vs. $\lambda_{\rm Edd}$ relation found in our sample with other samples of $L_{\rm bol} > 10^{47}$ erg s^{-1}) QSOs at lower z extending over wider ranges of $\lambda_{\rm Edd}$. We included the WISSH sample of QSOs at $z = 2-4$ from Zappacosta et al. (2020), the blue QSOs at $z \simeq 3.0-3.3$ selected from the SDSS DR7 from Trefoloni et al. (2023), the local hyper-Eddington accreting AGN ($1.2 \leq \lambda_{\rm Edd} \leq 468$, Tortosa et al. 2023), the radio-quiet AGN at $0.4 \leq z \leq 0.75$ accreting at $0.9 \leq \lambda_{\rm Edd} \leq 1.1$ (Laurenti et al. 2022), a sample of $z < 0.4$ AGN with reverberation mapping measurements which includes super-Eddington accreting AGN and sub-Eddington accreting AGN (Liu et al. 2021) and the sample of unobscured ($N_{\rm H} < 10^{22}$ cm^{-2}), radio quiet, type 1 AGN belonging to the Swift/BAT AGN Spectroscopic Survey (BASS) from Trakhtenbrot et al. (2017) with a median redshift of 0.035. Remarkably, ∼80% of the QSOs in our sample are located above the $\lambda_{\rm Edd}$ vs. Γ relations (see upper left panel of Figure 2 and Figure 7) presented in the literature for local AGN (e.g. Trakhtenbrot et al. 2017; Liu et al. 2021; Tortosa et al. 2023).

We note that the values of Γ in the different samples we obtained sampling different rest-frame energy ranges. However, the Γ values from the BASS sample (Ricci et al. 2017) and for the sample from Tortosa et al. (2023) were obtained at ≫10 keV rest-frame energies, similarly to the HYPERION sample. Furthermore, in Zappacosta et al. (2023), fits performed from 2 keV (i.e. rest-frame low-energy bound similar to that of the HYPERION QSOs), are reported for the WISSH QSOs analysed in

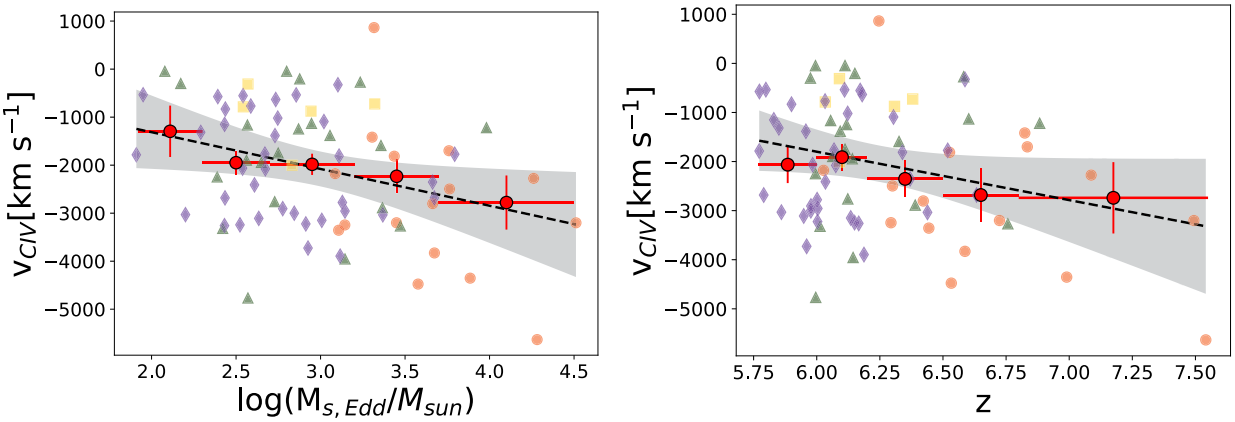

Fig. 8. Plot of the relations which do not involve X-ray data extending the data sample. Left panel: $v_{\rm C\,IV}$ vs. log($M_{\rm s,Edd}$) linear relation; Right panel: $v_{\rm C\,IV}$ vs. z linear relation. The orange circles and the yellow squares represent the HYPERION and non-HYPERION QSOs in our sample, respectively. The green triangles and the purple diamonds represent the QSOs from Farina et al. 2022 and Mazzucchelli et al. 2023, respectively. the red circles with errorbars correspond to the median value for each bin. The dashed black lines are the linear regressions while the shaded regions represent the combined 1σ error on the slope and normalization (see Table 6).

Zappacosta et al. (2020). The reported Γ values are comparable to those obtained also accounting for softer X-ray photons (<2 keV). This makes the comparison between the Γ measurements in different samples reliable, and strengthens the evidence for the steepening of the X-ray spectra of the first QSOs reported by Zappacosta et al. (2023).

We do not find a relation between $L_{\rm x}$ and $v_{\rm C\,IV}$ for the QSOs at $z > 6$ analysed in this work. We investigated this relation at a fixed UV luminosity (i.e. in a range smaller than ∼0.5 dex) as in Zappacosta et al. (2020). Thus, we excluded SDSS J0100+2802 because it is an outlier in terms of $L_{\rm bol}$ (see Table 1). At a fixed UV luminosity, luminous QSOs at Cosmic Noon show a $L_{\rm x}$ vs. $v_{\rm C\,IV}$ anti-correlation (Zappacosta et al. 2020). However, within the uncertainties, we are in agreement with the relation found by Zappacosta et al. (2020) (see upper right panel of Figure 2). We need to enlarge the dataset, to broaden the statistics and the interval of probed $v_{\rm C\,IV}$ and to test the presence of a $L_{\rm x}$ vs. $v_{\rm C\,IV}$ relation for $z > 6$ QSOs on a more solid basis.

5.3. Linking the X-ray corona with the SMBH mass growth history

We tested the Γ vs. log($M_{\rm s,Edd}$) and Γ vs. z relations, confirming, on a larger sample, the earlier claims by Zappacosta et al. (2023) of a Γ−$M_{\rm s,Edd}$ dependence. In our analysis we found these relations to be moderate, with <3σ significance, with the Γ−$M_{\rm s,Edd}$ dependence slightly more significant than that of the Γ−z. To check whether the Γ−z is affected by the potential selection bias of $z > 7$ QSOs we fitted the $6 < z < 7$ QSOs recovering a similar relation to what obtained when fitting the whole sample, with a slightly lower statistical significance (2.1σ). This suggests that the result is not influenced by the smaller $z > 7$ sample.

As argued in Zappacosta et al. 2023, the possibility that these sources experienced a redshift-dependent steepening of the spectra seems unlikely as it must happen in 0.2−0.3 Gyr (see lower right panel of Figure 2). This timescale is too short for any cosmological evolution to take place. The hypothesis that the steepening of Γ is dependent on $M_{\rm s,Edd}$ (i.e. driven by the fast SMBH growth experienced by these QSOs during their formation history) seems to be more likely.

However, Γ is an instantaneous quantity; it can quickly change in response to a change in the accretion state phase (e.g. Sobolewska & Papadakis 2009; Trakhtenbrot et al. 2017; Serafinelli et al. 2017). The existence of a tentative relation between $M_{\rm s,Edd}$, a proxy of the integrated growth history of the SMBH, is therefore intriguing. Between the two most popular pathways to grow $z > 6$ SMBHs, we consider the super Eddington growth as a more likely explanation of the relation with Γ as it is related to the accretion mechanism rather than to the initial seed BH mass. This would imply that these sources have been typically accreting at super-Eddington rates over their lifetime. This is at variance with their $\lambda_{\rm Edd}$ values, which are on average <1. Hence, it is possible that these sources have experienced a hybrid scenario whereby their growth is favoured by initial massive seeds and by a fast SMBH growth that is representative of the currently observed $\lambda_{\rm Edd}$.

The Γ vs. log($M_{\rm s,Edd}$) relation may not be a fundamental relation; rather, it is being derived from a third parameter that is by itself truly linked to $M_{\rm s,Edd}$. Furthermore, the existence of Γ vs. $v_{\rm C\,IV}$ and Γ vs. log($M_{\rm s,Edd}$) relations implies that $v_{\rm C\,IV}$ may depend on $M_{\rm s,Edd}$. We estimated a moderate significance (2.5σ, see Table 5) of the correlation between $v_{\rm C\,IV}$ and $M_{\rm s,Edd}$ in our sample. However the significance of this relation (which does not depend on the X-ray parameters) can be verified on a much larger sample of QSOs.

We also tested the relations between z, $M_{\rm s,Edd}$, and $v_{\rm C\,IV}$, which do not involve X-ray data, on an extended sample of ∼80 QSOs, which includes, along with the sources of this work, the sources with the most recent reliable $v_{\rm C\,IV}$ measurements derived by Farina et al. (2022) and Mazzucchelli et al. (2023) (see Figure 8). The sample from Farina et al. (2022) includes 31 bright QSOs at $5.78 < z < 7.54$, while the sample from Mazzucchelli et al. (2023) consists of 37 luminous QSOs at $z \geq 6$ with high signal-to-noise ratio VLT/X-shooter spectra (avoiding duplication with the HYPERION sample), acquired in the enlarged ESO Large Programme XQR-30 (P.I. D'Odorico, D'Odorico et al. 2023). For the comparison with our sample, we did not considered duplication in these samples. We applied the same fitting method described in Section 2 to the data. The best–fitting parameters for the $v_{\rm C\,IV}$vs. z and $v_{\rm C\,IV}$ vs. $M_{\rm s,Edd}$ relations are reported in Table 6. Figure 8 shows the plots of the relations we analysed in the extended sample. We also reported the median values computed in bins of $M_{\rm s,Edd}$ and z (red stars with errorbars in Figure 8). We chose to have the bins containing

Table 6. Best-fit relations for the extended sample analysed here with their correlation coefficients, null-hypothesis probabilities referred to the goodness of the fit and statistical significance.

Relation (y vs. x)			Slope (A)	Intercept (B)	Pearson	$1 - P_{\rm null}$	σ
$v_{\rm C\,IV}$	vs.	$\log(M_{\rm s,Edd})$	$(-7.94 \pm 2.45) \times 10^{+2}$	416 ± 73	-0.382	0.9988	3.04
$v_{\rm C\,IV}$	vs.	z	$(-9.81 \pm 4.24) \times 10^{+2}$	4193 ± 2654	-0.286	0.9868	2.22

at least five objects. The binned data exhibit the same trend of the fits. We found that, expanding the sample, the strength of the $v_{\rm C\,IV}$ vs. $M_{\rm s,Edd}$ relation increases and the statistical significance increases to 3σ (see left panel of Figure 8 and Table 6). We checked whether the $v_{\rm C\,IV}$ vs. $M_{\rm s,Edd}$ and the $v_{\rm C\,IV}$ vs. z relations are driven by the $z > 7$ QSOs subsample by excluding them from the fit of the extended sample (including the QSOs from Farina et al. 2022 and Mazzucchelli et al. 2023). We found relations that are completely in agreement within the errors with those obtained considering the total sample.

Past works analysing the average $v_{\rm C\,IV}$ of $z > 6$ QSOs, claimed a possible correlation between the $v_{\rm C\,IV}$ and z (Schindler et al. 2020; Yang et al. 2021). However, by considering the extended sample, which has a factor of 2.4 more sources than these samples, we found a marginal (2.2σ significance) correlation between $v_{\rm C\,IV}$ and z (see right panel of Figure 8, Table 6).

The existence of a more significant $M_{\rm s,Edd}$ dependence and the insufficient timescale argument could suggest that the real relation could be between $v_{\rm C\,IV}$ and $M_{\rm s,Edd}$. Furthermore, as postulated for the Γ vs. $\log(M_{\rm s,Edd})$ case, it is possible that the growth pathway for these sources includes a massive seed followed by high (but not super-Eddington) accretion rates (i.e. $\lambda_{\rm Edd} > 0.5$) for a significant time of the evolution during which powerful winds may be launched (Kubota & Done 2018; Jiang et al. 2019b; Okuda & Singh 2021; Luminari et al. 2021).

Finally, we note that the definition of $M_{\rm s,Edd}$ (see Equation (1)) involves a dependence on several parameters, including the details of the accretion flow; of the link between the AD-corona system; and of the link between the spin, the efficiency, and the possible impact from AD-driven outflows. A detailed examination of the interconnection among the various parameters involved within $M_{\rm s,Edd}$, along with a theoretical effort, is essential, but this is beyond the aim of this work.

6. Conclusions

We investigated the relations between the coronal X-ray properties, the velocities of the AD winds and the properties regarding the physics and growth of the AD and SMBH of a sample of luminous ($L_{\rm bol} > 10^{47}\,{\rm erg\,s^{-1}}$) QSOs at $z > 6$. The sample is composed of 16 sources belonging to the HYPERION sample (Zappacosta et al. 2023) and five QSOs from Connor et al. 2019, Vito et al. 2019, and Pons et al. 2020 for which high-quality X-ray observations and $v_{\rm C\,IV}$ measurements are available.

Our main finding can be summarized as follows:

- We find a significant ($>3\sigma$) anticorrelation between Γ and $v_{\rm C\,IV}$ (see Figure 1). This relation indicates a connection between the AD-corona configuration and the kinematics of AD winds. We explain it qualitatively in inner corona-outer AD models as a consequence of the transition between slim and standard discs at high accretion regimes. The formation of a inner geometrically puffed up AD (typical of high accretion flows) plays a role in producing steeper X-rays (as a consequence of coronal cooling induced by the high UV flux from this region) and in launching fast ionized AD winds from inner regions (which are shielded and hence not over-ionized by the central X-ray source flux).
- The QSOs in our sample and especially the HYPERION QSOs, generally show steeper X-ray continuum slopes compared to the canonical values, confirming the early claims (Vito et al. 2019; Wang et al. 2021b; Zappacosta et al. 2023) according to which the first QSOs have intrinsically different X-ray properties. Roughly 80% of the QSOs of the analysed sample is located above the $\lambda_{\rm Edd}$ vs. Γ relations (see upper left panel of Figure 2 and right panel of Figure 7) presented in the literature for local AGN (e.g. Trakhtenbrot et al. 2017; Liu et al. 2021; Tortosa et al. 2023). This is a further evidence of the steepening of the X-ray spectra of $z > 6$ QSOs. However, our data does not allow us to discriminate between a simple power law or a cut-off power law model. Because Γ and low $E_{\rm cut}$ are both tracers of relatively cold coronae, our result could suggest low coronal temperatures for the QSOs in our sample.
- We do not recover a statistically significant relation between $\lambda_{\rm Edd}$ and Γ in the QSOs in our sample (see upper left panel of Figure 2). However, we note that the analysed sample of QSOs allowed us to investigate a restricted range for $\lambda_{\rm Edd}$, with a limited number of $z > 6$ sources. Moreover, the $\lambda_{\rm Edd}$ parameters for the QSOs in our sample is located in the transition region between the standard geometrically thin AD and the geometrically thick AD. In this situation $\lambda_{\rm Edd}$ may not be a reliable proxy for the real accretion rate. All these prevented us from drawing firm conclusions on the existence of a relation between $\lambda_{\rm Edd}$ and Γ in the QSOs in our sample.
- We tested the link between $L_{\rm x}$ and $v_{\rm C\,IV}$, finding a mild relation (1.5σ, see upper right panel of Figure 2). Within the uncertainties, there is a marginal agreement with the trend of the relation found by Zappacosta et al. (2020), for a sample of analogous QSOs at Cosmic Noon. We need an expansion of the dataset, enhancing the statistics, to establish the existence of a $L_{\rm x}$ vs. $v_{\rm C\,IV}$ relation.
- A moderately significant dependence is found between Γ and z, and between Γ and $M_{\rm s,Edd}$, with a statistical significance of 2.3σ and 2.5σ, respectively (see lower panels of Figure 2). Given that a redshift evolution of Γ is highly unlikely to happen in the 0.2−0.3 Gyr corresponding to the redshift range in our sample (see lower right panel of Figure 2), a dependence with $M_{\rm s,Edd}$ is more likely. This could imply that these sources can preferentially acquire their large SMBH masses via accretion at high rates.
- Similarly to the previous relation, we report a significant anticorrelation also between $v_{\rm C\,IV}$ and $M_{\rm s,Edd}$ on a much larger sample regardless of their X-ray properties (see Figure 8).
- We report a significant ($>3\sigma$) ${\rm REW_{C\,IV}}$ vs. $v_{\rm C\,IV}$ anticorrelation in our sample of $z > 6$ (see Figure 3), confirming the well-established trend in lower-z QSOs (Richards et al. 2011; Shen & Ho 2014; Hamann et al. 2017; Vietri et al. 2018, 2020; Schindler et al. 2020; Matthews et al. 2023).

A future extensive examination of the relations presented in this work is fundamental, from the theoretical and the observational points of view. On one hand, a thorough theoretical analysis of the intricate connections among the different parameters involved in $M_{\rm s,Edd}$ it is necessary to establish the existence of a link between $M_{\rm s,Edd}$ and the SMBH mass growth history of high-z QSOs. On the other hand, it is crucial to expand the dataset by incorporating additional sources, especially those with a wider range of $M_{\rm s,Edd}$ values. To this end, we will take advantage of our recently accepted *XMM-Newton* Large programme observations (604 ks, P.I. L. Zappacosta) of more hyper-luminous QSOs at $z > 6$ significantly extending $M_{\rm s,Edd}$ at the lowest values, by more than doubling the number of sources with $M_{\rm s,Edd} < 1000\,M_{\odot}$. Moreover, we will jointly exploit state-of-the-art instrument (e.g. *Chandra*, JWST), possibly expanding the targets at even higher z (e.g. thanks to *Euclid*, Bogdán et al. 2024).

The next-generation X-ray observatory such as the Advanced X-Ray Imaging Satellite (AXIS, Reynolds et al. 2023) will be pivotal to determine the nature of the seeds of these earliest growing SMBH at $z > 6$ (e.g. Cappelluti et al. 2024). Moreover, the Wide Field Imager (WFI, Rau et al. 2013) large collecting area of the Advanced Telescope for High-Energy Astrophysics (*Athena*) mission, will play a crucial role by significantly minimizing the observing times. On the one hand this will increase the X-ray spectral quality and on the other hand it will permit the observation of more sources allowing a statistically more reliable characterization of the population of $z > 6$ QSOs.

Acknowledgements. This work is based on observations obtained with the ESA science mission *XMM-Newton*, with instruments and contributions directly funded by ESA Member States and the USA (NASA). We thank the *XMM-Newton* Science Operation Centre for the prompt support and advise for the scheduling and optimization of the *XMM*-HYPERION program. The authors acknowledge financial support from the Bando Ricerca Fondamentale INAF 2022 Large Grant "Toward an holistic view of the Titans: multi-band observations of $z > 6$ QSOs powered by greedy supermassive black holes" and the anonymous peer reviewer who generously dedicated their time and expertise to review and provide constructive feedback on this paper. LZ, EP, FN, AL acknowledge support from the HORIZON-2020 grant "Integrated Activities for the High Energy Astrophysics Domain" (AHEAD-2020), G.A. 871158. GM thanks grant PID2020-115325GB-C31 funded by MCIN/AEI/10.13039/501100011033 for support. FT and EP acknowledge funding from the European Union - Next Generation EU, PRIN/MUR 2022 2022K9N5B4. SC acknowledges support from the European Union (ERC, WINGS, 101040227). POP acknowledges financial support from the french national space agency (CNES) and the High Energy programme from the french National Centre for Scientific Research (PNHE/CNRS). AB, MB, SC, VD, FF, CF, SG, VT, MN, LZ acknowledge support from the European Union – Next Generation EU, PRIN/MUR 2022 2022TKPB2P – BIG-z. MB acknowledges support from INAF project 1.05.12.04.01 – MINI-GRANTS di RSN1 "Mini-feedback" and from UniTs under FVG LR 2/2011 project D55-microgrants23 "Hyper-gal". A very special thanks to the Hematology Department in the "Policlinico Umberto I" and to the Hematology Department and the Hematology Day Hospital in the "Policlinico Universitario Campus Bio-Medico". They saved my life and without them I would not have been able to complete this endeavor. I am grateful to my family, friends, and colleagues for their support and understanding especially throughout the last rough months.

References

Arnaud, K. A. 1996, ASP Conf. Ser., 101, 17
Bañados, E., Connor, T., Stern, D., et al. 2018, ApJ, 856, L25
Berton, M., Foschini, L., Ciroi, S., et al. 2015, A&A, 578, A28
Bogdán, Á., Goulding, A. D., Natarajan, P., et al. 2024, Nat. Astron., 8, 126
Boller, T., Brandt, W. N., & Fink, H. 1996, A&A, 305, 53
Brandt, W. N., Mathur, S., & Elvis, M. 1997, MNRAS, 285, L25
Cappelluti, N., Foord, A., Marchesi, S., et al. 2024, Universe, 10, 276
Cash, W. 1979, ApJ, 228, 939
Chehade, B., Carnall, A. C., Shanks, T., et al. 2018, MNRAS, 478, 1649
Chilingarian, I. V., Katkov, I. Y., Zolotukhin, I. Y., et al. 2018, ApJ, 863, 1
Coatman, L., Hewett, P. C., Banerji, M., & Richards, G. T. 2016, MNRAS, 461, 647
Collin, S., & Kawaguchi, T. 2004, A&A, 426, 797
Collin, S., Boisson, C., Mouchet, M., et al. 2002, A&A, 388, 771
Connor, T., Bañados, E., Stern, D., et al. 2019, ApJ, 887, 171
Connor, T., Bañados, E., Mazzucchelli, C., et al. 2020, ApJ, 900, 189
Czerny, B. 2019, Universe, 5, 131
De Rosa, G., Venemans, B. P., Decarli, R., et al. 2014, ApJ, 790, 145
Diamond-Stanic, A. M., Fan, X., Brandt, W. N., et al. 2009, ApJ, 699, 782
D'Odorico, V., Bañados, E., Becker, G. D., et al. 2023, MNRAS, 523, 1399
Eilers, A.-C., Simcoe, R. A., Yue, M., et al. 2023, ApJ, 950, 68
Elvis, M. 2000, ApJ, 545, 63
Fan, X., Strauss, M. A., Gunn, J. E., et al. 1999, ApJ, 526, L57
Fan, X., Bañados, E., & Simcoe, R. A. 2023, ARA&A, 61, 373
Farina, E. P., Schindler, J.-T., Walter, F., et al. 2022, ApJ, 941, 106
Faucher-Giguère, C.-A., & Quataert, E. 2012, MNRAS, 425, 605
Fiore, F., Feruglio, C., Shankar, F., et al. 2017, A&A, 601, A143
Gabriel, C., Denby, M., Fyfe, D. J., et al. 2004, ASP Conf. Ser., 314, 759
Gallerani, S., Zappacosta, L., Orofino, M. C., et al. 2017, MNRAS, 467, 3590
Greene, J. E., Strader, J., & Ho, L. C. 2020, ARA&A, 58, 257
Haardt, F., & Maraschi, L. 1991, ApJ, 380, L51
Haardt, F., & Maraschi, L. 1993, ApJ, 413, 507
Hamann, F., Zakamska, N. L., Ross, N., et al. 2017, MNRAS, 464, 3431
HI4PI Collaboration (Ben Bekhti, N., et al.) 2016, A&A, 594, A116
Inayoshi, K., Visbal, E., & Haiman, Z. 2020, ARA&A, 58, 27
Jiang, Y.-F., Blaes, O., Stone, J. M., & Davis, S. W. 2019a, ApJ, 885, 144
Jiang, Y.-F., Stone, J. M., & Davis, S. W. 2019b, ApJ, 880, 67
Jin, C., Done, C., & Ward, M. 2016, MNRAS, 455, 691
Jin, C., Done, C., & Ward, M. 2017, MNRAS, 468, 3663
Jin, C., Done, C., Ward, M., et al. 2023, MNRAS, 518, 6065
Johnson, J. L., & Haardt, F. 2016, PASA, 33, e007
Kaastra, J. S., & Bleeker, J. A. M. 2016, A&A, 587, A151
Kamraj, N., Brightman, M., Harrison, F. A., et al. 2022, ApJ, 927, 42
Kelly, B. C. 2007, ApJ, 665, 1489
Komossa, S., Voges, W., Xu, D., et al. 2006, ApJ, 132, 531
Kubota, A., & Done, C. 2018, MNRAS, 480, 1247
Kubota, A., & Done, C. 2019, MNRAS, 489, 524
Laurenti, M., Piconcelli, E., Zappacosta, L., et al. 2022, A&A, 657, A57
Leighly, K. M. 1999a, ApJS, 125, 297
Leighly, K. M. 1999b, ApJS, 125, 317
Leighly, K. M. 2004, ApJ, 611, 125
Leighly, K. M., & Moore, J. R. 2004, ApJ, 611, 107
Liu, H., Luo, B., Brandt, W. N., et al. 2021, ApJ, 910, 103
Luminari, A., Nicastro, F., Elvis, M., et al. 2021, A&A, 646, A111
Luo, B., Brandt, W. N., Hall, P. B., et al. 2015, ApJ, 805, 122
Lupi, A., Haardt, F., Dotti, M., et al. 2016, MNRAS, 456, 2993
Lusso, E., Nardini, E., Bisogni, S., et al. 2021, A&A, 653, A158
Madau, P., Haardt, F., & Dotti, M. 2014, ApJ, 784, L38
Maiolino, R., Scholtz, J., Witstok, J., et al. 2024, Nature, 630, E2
Marshall, M. A., Perna, M., Willott, C. J., et al. 2023, A&A, 678, A191
Marziani, P., Martínez Carballo, M. A., Sulentic, J. W., et al. 2016, Ap&SS, 361, 29
Matthews, J. H., Strong-Wright, J., Knigge, C., et al. 2023, MNRAS, 526, 3967
Mazzucchelli, C., Bañados, E., Venemans, B. P., et al. 2017, ApJ, 849, 91
Mazzucchelli, C., Bischetti, M., D'Odorico, V., et al. 2023, A&A, 676, A71
Meyer, R. A., Bosman, S. E. I., & Ellis, R. S. 2019, MNRAS, 487, 3305
Mezcua, M. 2017, Int. J. Mod. Phys. D, 26, 1730021P
Mineshige, S., Takeuchi, M., & Nishimori, H. 1994, ApJ, 435, L125
Miniutti, G., Fabian, A. C., Brandt, W. N., Gallo, L. C., & Boller, T. 2009, MNRAS, 396, L85
Miniutti, G., Brandt, W. N., Schneider, D. P., et al. 2012, MNRAS, 425, 1718
Mortlock, D. J., Warren, S. J., Venemans, B. P., et al. 2011, Nature, 474, 616
Nanni, R., Vignali, C., Gilli, R., Moretti, A., & Brandt, W. N. 2017, A&A, 603, A128
Nardini, E., Lusso, E., Risaliti, G., et al. 2019, A&A, 632, A109
Ni, Q., Brandt, W. N., Luo, B., et al. 2018, MNRAS, 480, 5184
Okuda, T., & Singh, C. B. 2021, MNRAS
Plotkin, R. M., Anderson, S. F., Brandt, W. N., et al. 2010, AJ, 139, 390
Pons, E., McMahon, R. G., Simcoe, R. A., et al. 2019, MNRAS, 484, 5142
Pons, E., McMahon, R. G., Banerji, M., & Reed, S. L. 2020, MNRAS, 491, 3884
Pounds, K. A., Done, C., & Osborne, J. P. 1995, MNRAS, 277, L5
Rankine, A. L., Hewett, P. C., Banerji, M., & Richards, G. T. 2020, MNRAS, 492, 4553
Rau, A., Meidinger, N., & Nandra, K. 2013, ArXiv e-prints [arXiv:1308.6785]
Reed, S. L., Banerji, M., Becker, G. D., et al. 2019, MNRAS, 487, 1874
Reines, A. E., Greene, J. E., & Geha, M. 2013, ApJ, 775, 116
Reynolds, C. S., Kara, E. A., Mushotzky, R. F., et al. 2023, SPIE, 12678, 126781E

Ricci, C., Trakhtenbrot, B., Koss, M. J., et al. 2017, ApJS, 233, 17
Richards, G. T., Vanden Berk, D. E., Reichard, T. A., et al. 2002, AJ, 124, 1
Richards, G. T., Lacy, M., Storrie-Lombardi, L. J., et al. 2006, ApJS, 166, 470
Richards, G. T., Kruczek, N. E., Gallagher, S. C., et al. 2011, AJ, 141, 167
Sadowski, A. 2011, ArXiv e-prints [arXiv:1108.0396]
Sądowski, A., & Narayan, R. 2016, MNRAS, 456, 3929
Salvestrini, F., Risaliti, G., Bisogni, S., Lusso, E., & Vignali, C. 2019, A&A, 631, A120
Schindler, J.-T., Farina, E. P., Bañados, E., et al. 2020, ApJ, 905, 51
Serafinelli, R., Vagnetti, F., & Middei, R. 2017, A&A, 600, A101
Shakura, N. I., & Sunyaev, R. A. 1973, A&A, 24, 337
Shen, Y., & Ho, L. C. 2014, Nature, 513, 210
Shen, Y., Richards, G. T., Strauss, M. A., et al. 2011, ApJS, 194, 45
Shen, Y., Brandt, W. N., Richards, G. T., et al. 2016, ApJ, 831, 7
Shen, Y., Wu, J., Jiang, L., et al. 2019, ApJ, 873, 35
Sobolewska, M. A., & Papadakis, I. E. 2009, MNRAS, 399, 1597
Strüder, L., Briel, U., Dennerl, K., et al. 2001, A&A, 365, L18
Sulentic, J. W., Marziani, P., & Dultzin-Hacyan, D. 2000, ARA&A, 38, 521
Sulentic, J. W., Marziani, P., Zamanov, R., et al. 2002, ApJ, 566, L71
Sunyaev, R. A., & Titarchuk, L. G. 1980, A&A, 86, 121
Temple, M. J., Banerji, M., Hewett, P. C., Rankine, A. L., & Richards, G. T. 2021, MNRAS, 501, 3061
Timlin, J. D., Brandt, W. N., Ni, Q., et al. 2020, MNRAS, 492, 719
Tortosa, A., Ricci, C., Ho, L. C., et al. 2023, MNRAS, 519, 6267
Trakhtenbrot, B., Ricci, C., Koss, M. J., et al. 2017, MNRAS, 470, 800
Travascio, A., Zappacosta, L., Cantalupo, S., et al. 2020, A&A, 635, A157
Trefoloni, B., Lusso, E., Nardini, E., et al. 2023, A&A, 677, A111
Turner, M. J. L., Abbey, A., Arnaud, M., et al. 2001, A&A, 365, L27
Valiante, R., Schneider, R., Volonteri, M., & Omukai, K. 2016, MNRAS, 457, 3356
Valiante, R., Agarwal, B., Habouzit, M., & Pezzulli, E. 2017, PASA, 34, e031
Vestergaard, M., & Osmer, P. S. 2009, ApJ, 699, 800
Vietri, G., Piconcelli, E., Bischetti, M., et al. 2018, A&A, 617, A81
Vietri, G., Mainieri, V., Kakkad, D., et al. 2020, A&A, 644, A175
Vito, F., Brandt, W. N., Bauer, F. E., et al. 2019, A&A, 630, A118
Vito, F., Brandt, W. N., Ricci, F., et al. 2021, A&A, 649, A133
Volonteri, M. 2010, A&ARv, 18, 279
Wachter, K., Leach, R., & Kellogg, E. 1979, ApJ, 230, 274
Wang, F., Davies, F. B., Yang, J., et al. 2020, ApJ, 896, 23
Wang, F., Fan, X., Yang, J., et al. 2021a, ApJ, 908, 53
Wang, F., Yang, J., Fan, X., et al. 2021b, ApJ, 907, L1
Wills, B. J., Shang, Z., & Yuan, J. M. 2000, New Astron. Rev., 44, 511
Wu, J., Brandt, W. N., Hall, P. B., et al. 2011, ApJ, 736, 28
Wu, J., Brandt, W. N., Anderson, S. F., et al. 2012, ApJ, 747, 10
Wu, X.-B., Wang, F., Fan, X., et al. 2015, Nature, 518, 512
Yang, J., Wang, F., Fan, X., et al. 2020, ApJ, 897, L14
Yang, J., Wang, F., Fan, X., et al. 2021, ApJ, 923, 262
Yang, J., Fan, X., Wang, F., et al. 2022, ApJ, 924, L25
Yang, J., Wang, F., Fan, X., et al. 2023, ApJ, 951, L5
Zappacosta, L., Piconcelli, E., Giustini, M., et al. 2020, A&A, 635, L5
Zappacosta, L., Piconcelli, E., Fiore, F., et al. 2023, A&A, 678, A201

[1] INAF – Osservatorio astronomico di Roma, Via Frascati 33, I-00040 Monte Porzio Catone, Italy
[2] INAF – Osservatorio Astronomico di Trieste, Via G. Tiepolo 11, I-34143 Trieste, Italy
[3] Dipartimento di Fisica, Sezione di Astronomia, Università di Trieste, Via Tiepolo 11, I-34143 Trieste, Italy
[4] Centre for Extragalactic Astronomy, Department of Physics, Durham University, South Road, Durham DH1 3LE, UK
[5] Centro de Astrobiología (CAB), CSIC-INTA, Camino Bajo del Castillo s/n, ESAC campus, 28692 Villanueva de la Cañada, Spain
[6] Dipartimento di Matematica e Fisica, Università Roma Tre, Via della Vasca Navale 84, 00146 Roma, Italy
[7] INAF – Istituto di Astrofisica Spaziale e Fisica Cosmica Milano, Via A. Corti 12, 20133 Milano, Italy
[8] Dipartimento di Fisica e Astronomia 'Augusto Righi', Universitá degli Studi di Bologna, Via P. Gobetti, 93/2, 40129 Bologna, Italy
[9] INAF – Osservatorio di Astrofisica e Scienza dello Spazio di Bologna, Via Piero Gobetti, 93/3, I-40129 Bologna, Italy
[10] Scuola Normale Superiore, Piazza dei Cavalieri 7, I-56126 Pisa, Italy
[11] NASA Goddard Space Flight Center, Greenbelt, MD 20771, USA
[12] IFPU – Institute for Fundamental Physics of the Universe, Via Beirut 2, I-34151 Trieste, Italy
[13] INFN – National Institute for Nuclear Physics, Via Valerio 2, I-34127 Trieste, Italy
[14] Center for Astrophysics – Harvard & Smithsonian, Cambridge, MA 02138, USA
[15] Steward Observatory, University of Arizona, Tucson, AZ, USA
[16] INAF – Osservatorio Astronomico di Padova, Vicolo dell'Osservatorio 5, I-35122 Padova, Italy
[17] European Space Agency, ESTEC, Keplerlaan 1, 2201, AZ Noordwijk, The Netherlands
[18] DiSAT, Università degli Studi dell'Insubria, Via Valleggio 11, I-22100 Como, Italy
[19] INFN – Sezione di Milano-Bicocca, Piazza della Scienza 3, I-20126 Milano, Italy
[20] INAF – Osservatorio Astronomico di Brera, Via E. Bianchi 46, I-23807 Merate, Italy
[21] INAF – Istituto di Astrofisica e Planetologia Spaziali, Via del Fosso del Caveliere 100, I-00133 Roma, Italy
[22] Cavendish Laboratory, University of Cambridge, 19 J. J. Thomson Ave., Cambridge CB3 0HE, UK
[23] Kavli Institute for Cosmology, University of Cambridge, Madingley Road, Cambridge CB3 0HA, UK
[24] Department of Physics & Astronomy, University College London, Gower Street,, London WC1E 6BT, UK
[25] Univ. Grenoble Alpes, CNRS, IPAG, F-38000 Grenoble, France
[26] ASI – Agenzia Spaziale Italiana, Via del Politecnico snc, I-00133 Roma, Italy
[27] Dipartimento di Fisica, Università di Roma La Sapienza, Piazzale Aldo Moro 2, I-00185 Roma, Italy
[28] INFN – Sezione Roma1, Dipartimento di Fisica, Università di Roma La Sapienza, Piazzale Aldo Moro 2, I-00185 Roma, Italy
[29] Sapienza School for Advanced Studies, Viale Regina Elena 291, I-00161 Roma, Italy
[30] Physics Department, Tor Vergata University of Rome, Via della Ricerca Scientifica 1, 00133 Rome, Italy
[31] INFN – Rome Tor Vergata, Via della Ricerca Scientifica 1, 00133 Rome, Italy
[32] Department of Astronomy, University of Maryland, College Park, MD 20742, USA
[33] University of Ljubljana, Department of Mathematics and Physics, Jadranska ulica 19, SI-1000 Ljubljana, Slovenia
[34] Main Astronomical Observatory, National Academy of Sciences of Ukraine, 27 Akademika Zabolotnoho St., Kyiv 03143, Ukraine
[35] Institut d'Astrophysique de Paris, Sorbonne Université, CNRS, UMR 7095, 98 bis bd Arago, 75014 Paris, France